

Opto-mechanical manipulation of indium atoms

Dissertation

zur

Erlangung des Doktorgrades (Dr. rer. nat.)

der

Mathematisch-Naturwissenschaftlichen Fakultät

der

Rheinischen Friedrich-Wilhelms-Universität Bonn

vorgelegt von

Jiayu Wang

aus

Shanghai, China

Bonn 2004

Angefertigt mit Genehmigung der Mathematisch-Naturwissenschaftlichen Fakultät der
Rheinischen Friedrich-Wilhelms-Universität Bonn

1. Referent: Prof. Dr. Dieter Meschede
2. Referent: Prof. Dr. Karl Maier

Tag der Promotion: 23.07.2004

Die Vorliegende Arbeit wurde in der Zeit von Oktober 1999 bis Dezember 2003 am Institut für Angewandte Physik der Universität Bonn unter der Leitung von Prof. Dr. Dieter Meschede durchgeführt.

Mein besonderer Dank gilt Prof. Dr. Dieter Meschede für Ihre Unterstützung, Ihre stetige Diskussionsbereitschaft und vor allem Ihre zahlreichen Anregungen die sehr zum Gelingen dieser Arbeit beigetragen haben.

Ebenso möchte ich mich an dieser Stelle bei Prof. Dr. Karl Maier für die freundliche Übernahme des Korreferentes bedanken.

With Love and Affection for

My Wife, Son and Parents

Contents

1	Introduction	1
2	Basic principles	3
2.1	Indium	3
2.2	Laser cooling	4
2.3	Atom focusing	7
3	Apparatus	13
3.1	GaN diode laser	13
3.2	Frequency doubled Ti:Sapphire laser	14
3.2.1	Ti:Sapphire laser	14
3.2.2	Second harmonic generation (SHG)	15
3.2.3	Phase matching	16
3.2.4	Lithiumtriborate (LBO)	17
3.2.5	Boyd-Kleinman theory	19
3.2.6	Single-pass frequency doubling	20
3.2.7	Resonator enhancement	21
3.2.8	Mode matching	23
3.2.9	Impedance matching and power enhancement	23
3.2.10	Hänsch-Couillaud stabilization	25
3.2.11	Performance of the SHG resonator	28
3.3	Multi-frequency generation at 451 nm	30
3.4	Vacuum system	30
4	Spectroscopy and frequency stabilization	33
4.1	Atomic sources	33
4.1.1	Hollow cathode	33
4.1.2	All sapphire cell	34
4.2	Absorption spectroscopy	35
4.3	Saturation spectroscopy	37

4.4	Polarization spectroscopy	39
4.5	Fluorescence spectroscopy	41
4.6	Frequency stabilization	42
4.6.1	Allan variance	42
4.6.2	Frequency stabilization of the diode lasers	43
4.7	Two color spectroscopy	45
5	Opto-mechanical manipulation of an indium atomic beam	49
5.1	Experimental set-up	49
5.2	Experimental observations	50
5.2.1	Opto-mechanical effects with 410 nm and 451 nm lasers	51
5.2.1.1	Red-detuned 410 nm and 451 nm lasers	51
5.2.1.2	Blue-detuned 410 nm and 451 nm lasers	52
5.2.2	Opto-mechanical effects with two 410 nm lasers	52
5.2.3	Opto-mechanical effects with one 410 nm laser	53
5.2.3.1	$F = 4 \rightarrow 5$ cooling transition	54
5.2.3.2	$F = 5 \rightarrow 5$ and $F = 5 \rightarrow 4$ cooling transitions	55
5.3	Discussion of the possible mechanisms	57
5.3.1	Stimulated emission cooling	57
5.3.2	Adiabatic cooling	59
5.3.3	Bichromatic cooling	59
5.4	Discussion of achieving Doppler cooling	60
6	Summary and outlook	63
A	Transition strengths	65
B	Zeeman splitting	69
C	Indium data	71
	References	73
	Acknowledgements	79

Chapter 1

Introduction

Atom optics dates back to the famous experiments by Stern and Gerlach in 1920's [1, 2]. However, its rapid development started from the advent of laser cooling in 1975 [3, 4]. It realizes the manipulation of the motion of free, neutral atoms using forces arising from the interaction between atoms and light fields. Since then, many different methods of laser cooling have been developed [5, 6]. Laser cooling provides an important method for the preparation of well-collimated, intense atomic beams with a well-defined velocity and de Broglie wavelength [7].

Atom optics is now being applied in a variety of fields. One of these is the production of patterns and structures on suitable surfaces in nanometer scale. This process is called atom lithography which was invented at Bell Laboratories in 1992 [8]. Compared with other conventional types of lithography, non-conventional atom lithography is a parallel process which enables fast structuring and production in large dimensions. Furthermore, this method uses the direct deposition of atoms on the substrates and removes the photore-sist and the etch processes. So far one- [8], two- [9, 10] and three-dimensional structures [11] have been produced.

As an element of group III, indium is technologically attractive especially in the semi-conductor and optoelectronics fields. In this thesis, as the first and an important step towards the atom lithography with indium, the opto-mechanical manipulation of the indium atomic beam is demonstrated. In chapter two, the basic theory of the laser cooling and atom focusing is introduced. Due to the complicated atomic structure of indium, two wavelengths at 410 nm and 451 nm are necessary for the manipulation. The preparation of the appropriate light sources is introduced in chapter three. In chapter four the stabilization of the laser frequencies on an atomic reference with the spectroscopic method is discussed. In chapter five the opto-mechanical manipulation of an indium atomic beam is experimentally demonstrated and the possible mechanisms are discussed as well.

Chapter 2

Basic principles

2.1 Indium

Indium is a very soft, silvery white metal with a brilliant luster, and stable both in air and in water. As an element of group III, it is chemically similar to Aluminum or Gallium.

The atomic number of indium amounts to 49, its atomic weight is 114.82. The melting point and boiling point are 156.61 °C and 2080 °C, respectively [12]. Its vapor pressure can be described by the following empirical expression [13]:

$$\lg P(Torr) = 8.003 - \frac{12180}{T}, \quad (2.1)$$

where T is the absolute temperature in Kelvin. At a temperature of 1200 °C, the vapor pressure reaches 10 mTorr.

Indium has two stable isotopes ^{113}In and ^{115}In with an abundance of 4.3 % and 95.7 %, respectively. Both isotopes have a nuclear spin of $I = 9/2$.

The electronic configuration of indium atom in the ground state $^2P_{1/2}$ is $[Kr] 4d^{10} 5s^2 5p$. The energy level diagram of the dominant isotope ^{115}In is shown in Figure 2.1. ^{113}In has a similar energy level which is red shifted by 258.2 MHz [14]. The $5^2P_{1/2} \rightarrow 6^2S_{1/2}$ and $5^2P_{3/2} \rightarrow 6^2S_{1/2}$ transitions have a wavelength of 410.29 nm and 451.26 nm in vacuum, respectively. For the calculation of the natural linewidth one must notice that the atoms in the $6^2S_{1/2}$ level can decay to both $5^2P_{1/2}$ level and $5^2P_{3/2}$ level, so the total decay rate is given by $A_{tot} = A_1 + A_2$, where A_1 and A_2 are [15]

$$\begin{aligned} 6^2S_{1/2} \rightarrow 5^2P_{1/2} & : A_1 = 0.56 \cdot 10^8 \text{ s}^{-1} = 2\pi \cdot 8.9 \text{ MHz} \\ 6^2S_{1/2} \rightarrow 5^2P_{3/2} & : A_2 = 1.02 \cdot 10^8 \text{ s}^{-1} = 2\pi \cdot 16.2 \text{ MHz} . \end{aligned} \quad (2.2)$$

The natural linewidth is then calculated to be

$$\Gamma = A_{tot} = 2\pi \cdot 25.1 \text{ MHz} , \quad (2.3)$$

and the lifetime of the $6^2S_{1/2}$ level is

$$\tau = \frac{1}{\Gamma} = 6.33 \text{ ns} . \quad (2.4)$$

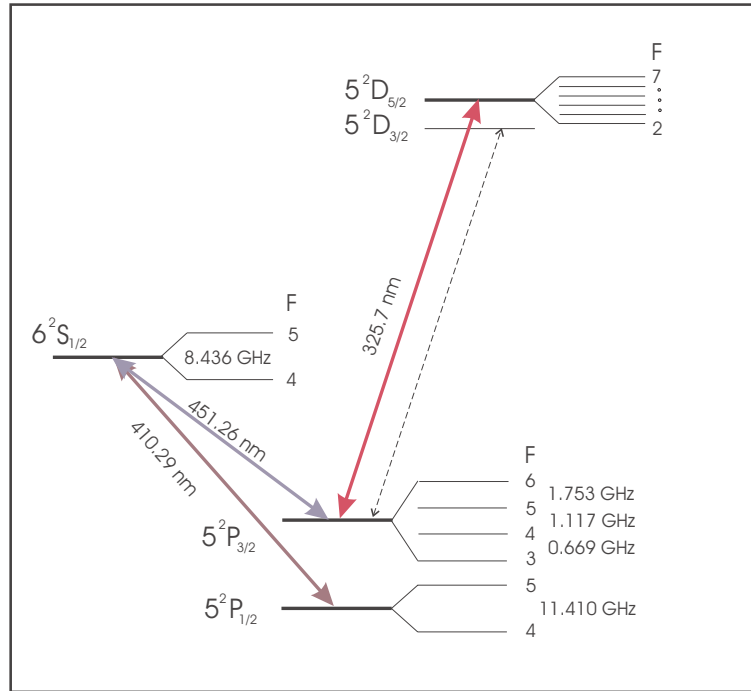


Figure 2.1: Diagram of lower-lying energy levels in indium, including the hyperfine structure. The marked wavelengths are wavelengths in vacuum.

2.2 Laser cooling

In 1975 two groups, Hänsch and Schawlow at Stanford University [3] and Wineland and Dehmelt at the University of Washington [4], independently introduced the idea of laser cooling. In Hänsch and Schawlow’s paper titled as “Cooling of gases by laser radiation”, the cooling mechanism was attributed to the Doppler effect which makes the radiation pressure on an atom velocity dependent. This cooling mechanism is known as Doppler cooling.

Consider a two-level atom with a frequency interval between ground and excited states of ω_0 . This atom is irradiated by a laser beam of frequency ω and wavelength λ . Each

photon of the laser carries a momentum $\hbar k$, where $k = \frac{2\pi}{\lambda}$ is the wave vector. For an atom moving in the positive x direction, it experiences an average force which is the photon momentum times the average rate of absorbing photons γ_{abs} (Figure 2.2):

$$\begin{aligned} F_{\pm} &= \pm \hbar k \gamma_{abs} \\ &= \pm \hbar k \frac{\Gamma}{2} \frac{s_0}{1 + s_0 + [(\Delta \mp kv)/(\Gamma/2)]^2}, \end{aligned} \quad (2.5)$$

where Γ is the linewidth of the transition, $\Delta = \omega - \omega_0$ is the detuning of the laser, kv is the Doppler shift and $s_0 = I/I_{sat}$ is the saturation parameter. Here the plus (minus) sign refers to the force from the laser beam propagating in the positive (negative) x direction. This force is usually called the radiation pressure force.

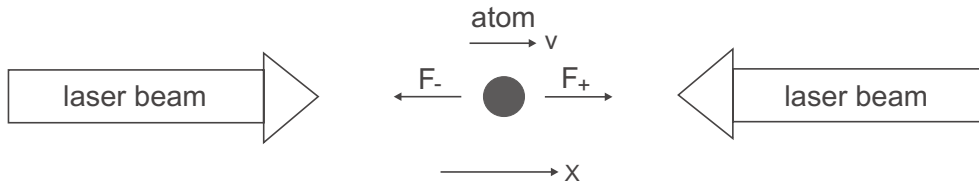


Figure 2.2: Radiation pressure force on the atom.

Now we apply a pair of counterpropagating laser beams and assume that these two beams act independently on the atoms ($s_0 < 1$), the average force on the atom is then written as

$$F = F_+ + F_- . \quad (2.6)$$

Red-detuning the laser frequency from resonance ($\Delta < 0$), the atoms moving in the opposite direction of propagation of the laser beam are more likely to absorb photons than the ones moving along the direction of the laser beam due to the Doppler effect, and gain consequently a recoil momentum from the laser. The result is that atoms experience a friction force and their velocities are reduced. Meanwhile, their kinetic energy is supplied by heating from the random nature of the spontaneous emission. As a result, the minimum achievable temperature T_D with Doppler cooling is [16]

$$k_B T_D = \hbar \Gamma / 2 , \quad (2.7)$$

where k_B is the Boltzmann constant. This is the so called Doppler-cooling limit which is $600 \mu K$ for indium. This temperature is obtained when the cooling laser is detuned by $\Gamma/2$. The velocity capture range Δv is then

$$\Delta v \sim \Gamma / k . \quad (2.8)$$

In 1989 two groups, Dalibard and Cohen-Tannoudji at the Ecole Normale Supérieure [5] and Chu et al [6] at Stanford University, proposed a new cooling mechanism which relies

on polarization gradients to explain their observed temperature lower than the Doppler cooling limit. Later, there are other cooling mechanisms being investigated. Some of them will be discussed in chapter 5.3.

Since Doppler cooling utilizes the very small momentum of laser photons, the atomic velocity changes little for each absorption of one photon. For indium atoms irradiated by 410 nm and 451 nm laser, each absorption reduces their velocity by 8.5 mm/s and 7.7 mm/s, respectively. The atoms must repeat as many absorption-emission cycles as possible to change their velocity substantially. Thus, a closed atomic transition system is necessary. The indium level diagram shows that the $5^2P_{3/2}$ ($F=6$) \rightarrow $5^2D_{5/2}$ ($F=7$) transition at 325.7 nm can be directly used for this purpose. However, due to a low thermal population of 6.5 % in the $5^2P_{3/2}$ ($F=6$) level at a temperature of 1200 °C, both the 410 nm and 451 nm light must be used to optically pump the atoms from the $5^2P_{1/2}$ ($F=4, 5$) levels and the $5^2P_{3/2}$ ($F=3, 4, 5$) levels to the $5^2P_{3/2}$ ($F=6$) level.

As an alternative one can utilize the $5^2P_{1/2}$ ($F=4, 5$) \rightarrow $6^2S_{1/2}$ ($F=5$) transitions at 410 nm and $5^2P_{3/2}$ ($F=4, 5, 6$) \rightarrow $6^2S_{1/2}$ ($F=5$) transitions at 451 nm for laser cooling. Here the atoms in the $5^2P_{3/2}$ ($F=3$) are neglected, because there is only a thermal population of 3.5 % in this level at a temperature of 1200 °C. This Λ -type cooling scheme eliminates the usage of a 325.7 nm laser and opens up a new possibility to cool the atoms using two different wavelengths.

In order to get an estimation of the laser cooling, a numerical simulation is performed. We use the simplest one-dimensional Doppler cooling as the cooling model. In the simulation, the 410 nm laser is the red-detuned cooling laser and the 451 nm laser is set on resonance. In addition, for simplicity, it is assumed that the initial atomic transverse velocities are Gaussian distributed with a standard deviation of 5 m/s, and the longitudinal velocities have a Maxwell-Boltzmann distribution with a most probable velocity of 565 m/s corresponding to an oven temperature of 1200 °C. All other parameters including the initial atomic velocity, angle and decay channels are randomly generated.

Figure 2.3(a) illustrates a Gaussian distribution of the initial transverse velocities with a standard deviation of 5 m/s. In the simulation, the cooling laser has a power of 4 mW and a Gaussian beam profile with a waist ($1/e^2$ radius) of 3 mm, corresponding to a maximum saturation parameter of $s_0=0.6$ and an interaction length of roughly 6 mm between the atoms and the cooling laser. By setting the cooling laser red detuned by half of the natural linewidth, the standard deviation of the transverse velocities reduces to 0.28 m/s. (see Figure 2.3(b)). The number of the atoms near zero velocity increases by a factor of 4.5 after laser cooling.

We have also investigated the transverse velocity distribution after laser cooling for different detunings of the cooling laser. Figure 2.4 shows the standard deviation of the

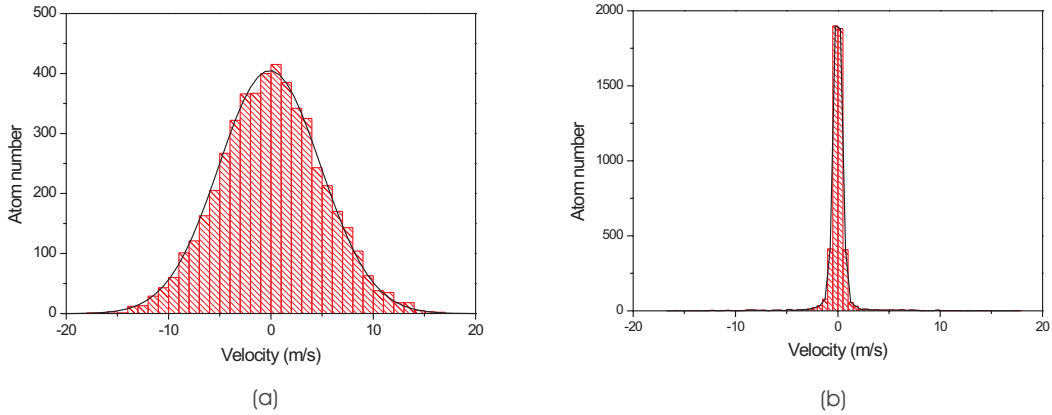


Figure 2.3: *Distribution of the transverse velocity of the atoms (a) before Doppler cooling with a standard deviation of 5 m/s and (b) after laser cooling with a standard deviation of 0.28 m/s. The solid curves are the Gaussian fit. The cooling lasers are red detuned by half of the natural linewidth and have a power of 4 mW. The interaction length between the indium atoms and the laser fields is roughly 6 mm.*

transverse atomic velocities for different detunings of the Gaussian cooling laser with a power of 4 mW and a waist of 3 mm. The interaction length is therefore roughly 6 mm. With the increase of the detuning, the deviation decreases at first, then reaches a small plateau followed by an increase at larger detuning. The small plateau lies at a detuning roughly between -12 MHz and -14 MHz which corresponds to the expected optimum value around $-\Gamma/2 = 2\pi \cdot (-12.5)$ MHz. The minimum transverse velocity spread of 28 cm/s coincides with the theoretical value derived from the Doppler cooling theory.

2.3 Atom focusing

Besides the velocity-dependent radiation pressure force, there is another form of force between light and atoms. It arises from the interaction between the induced atomic dipole moment with a gradient in the electric field of the laser, and is therefore often referred to as the dipole force [17]. The dipole force on a two-level atom is derived from an optical potential which can approximately be written as [18]

$$U(x, y, z) = \frac{\hbar\Delta}{2} \ln[1 + p(x, y, z)] . \quad (2.9)$$

Here

$$p(x, y, z) = \frac{I(x, y, z)}{I_{sat}} \frac{\Gamma^2}{\Gamma^2 + 4\Delta^2} , \quad (2.10)$$

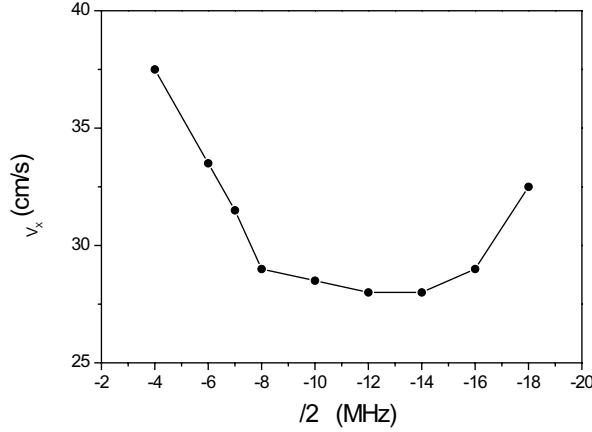


Figure 2.4: Standard deviation of transverse atomic velocities for different detunings of the cooling laser having a power of 4 mW. The interaction length between the indium atoms and the laser fields is roughly 6 mm.

where $I(x, y, z)$ is the spatial distribution of the laser intensity. For an one-dimensional standing-wave laser field along the x axis, the spatial distribution is

$$I(x, y, z) = I_0 e^{-\frac{2z^2}{\sigma_z^2}} \sin^2 kx, \quad (2.11)$$

where σ_z is the waist ($1/e^2$ radius) of the Gaussian laser beam along z direction and I_0 is the maximum laser intensity. Any y -dependence of the laser intensity is ignored because the light force along this direction is negligible compared with those resulting from the standing wave.

The idea of using light forces for nanofabrication was first proposed in 1987 by Balykin and Letokhov [19]. Later, McClelland and Timp *et al.* theoretically analyzed the laser focusing of neutral atoms using the atom optics approach [18, 20]. In 1992, laser focusing of neutral atoms into an array of narrow parallel lines was first demonstrated by Timp *et al.* at Bell labs [8]. They used a one-dimensional standing wave of laser light as a light mask, which acts as an array of cylindrical lenses, to focus a beam of Na atoms into parallel lines during deposition onto a Si substrate [21]. Similarly, McClelland *et al.* focused Cr atoms onto a substrate by using a standing wave [22].

A typical scheme of one-dimensional atom focusing is shown in Figure 2.5. A laser beam is directed across the surface of a substrate along the x axis and retroflected by a mirror to generate a standing wave. A collimated beam of atoms is incident perpendicular to the surface along the z direction. The frequency of the standing wave is detuned

relative to an atomic transition frequency so that the standing wave acts as a periodic array of cylindrical lenses for atoms with a period of half of the laser wavelength. The atoms experience a transverse light force while travelling through the standing wave and are focused into narrow lines during deposition onto the substrate. For a blue-detuned standing wave, the atoms are attracted to the nodes. The achieved lines have intervals of half the laser wavelength and the linewidths typically are around $\lambda/10 \sim \lambda/20$.

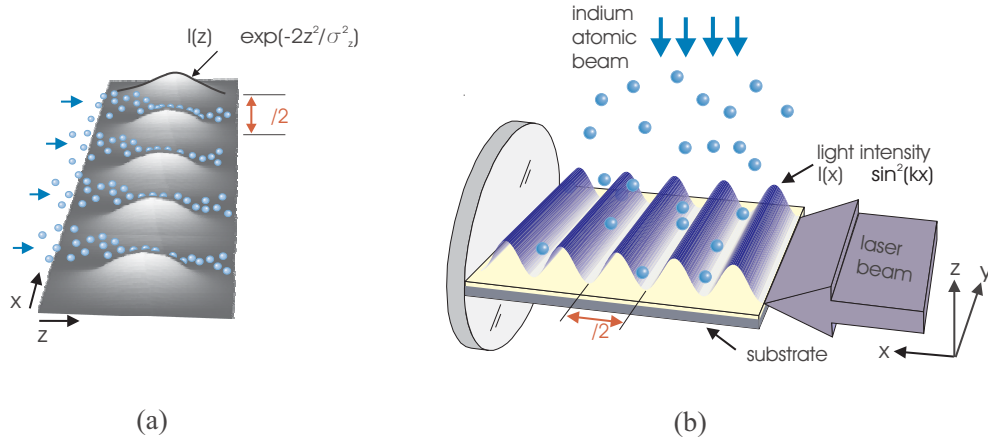


Figure 2.5: *One-dimensional atom focusing in a standing wave acting as an array of cylindrical lenses. The intensity of the standing wave has a Gaussian envelope along z direction (a) and a sinusoidal distribution along x direction (b).*

The simulation of the atom focusing is performed with indium atoms. The Gaussian laser beam used to generate the standing-wave has a power of 4 mW and a waist ($1/e^2$ radius) of $720 \mu\text{m}$ along y direction and $100 \mu\text{m}$ along z direction, respectively, corresponding to a maximum saturation parameter of $s_0 = 75$. The frequency of the standing-wave is detuned relative to the $F = 4 \rightarrow 5$ transition at 410 nm. The detuning is adjusted so that the focus of the light lenses lies on the surface of the substrate at $z=0$ where is the middle of the Gaussian beam. At first, for simplicity, we assume that the atoms have a zero transverse spread in x direction and a monochromatic longitudinal velocity of 565 m/s. Figure 2.6 (a) shows a series of atomic trajectories for different incident positions with a detuning of 5.7Γ and an interaction length of roughly $100 \mu\text{m}$. At the focal plane a very narrow flux peak with a width of 1 nm is observed (see Figure 2.6 (b)).

Next, we keep the monochromatic longitudinal velocity and use the transverse spread having a Gaussian distribution with a deviation of 28 cm/s which is obtained from the simulation of the laser cooling. It shows a flux peak having a broad width of 50 nm at the focal plane (see Figure 2.7(a)). Finally, we use the Maxwell-Boltzmann distributed longitudinal velocity and Gaussian distributed transverse velocity. It shows a flux peak of a width of 58 nm (see Figure 2.7 (b)). From the simulation we can conclude that the

width of the flux peak is primarily determined by the transverse spread of the atomic beam. Thus, laser cooling to at least the Doppler limit is important.

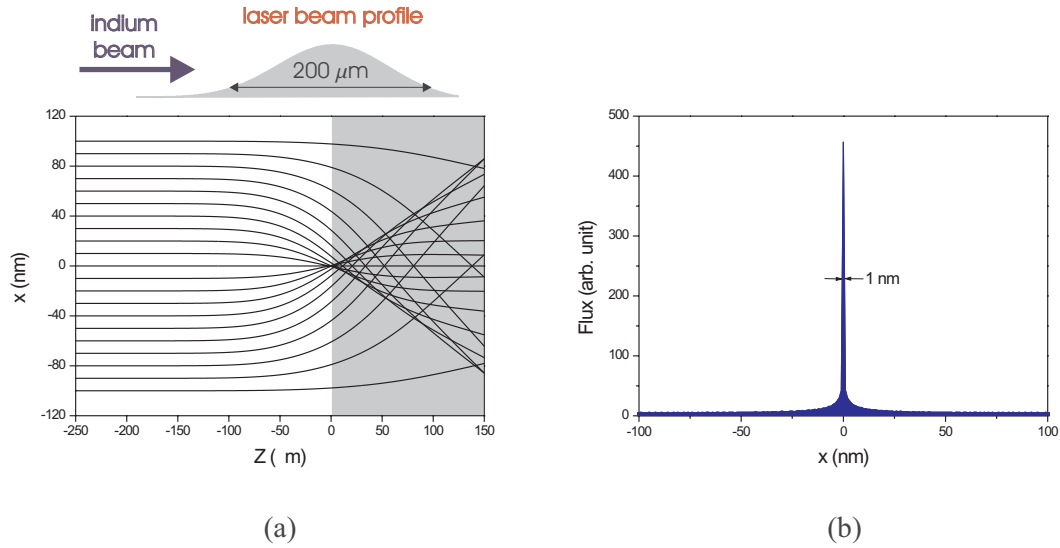


Figure 2.6: (a) Trajectory of indium atoms travelling in a blue-detuned standing wave with a Gaussian envelope of a $100\ \mu\text{m}$ waist along z direction within one period. The gray area represents the substrate whose surface locates in the middle of the Gaussian beam. The laser beam used to generate the standing wave has a maximum saturation parameter of $s_0 = 75$ and its frequency is blue detuned relative to the $F = 4 \rightarrow 5$ transition at $410\ \text{nm}$ by $\Delta = 5.7\Gamma$. The interaction length between the atoms and laser field is roughly $100\ \mu\text{m}$. (b) The atomic flux at the focal plane.

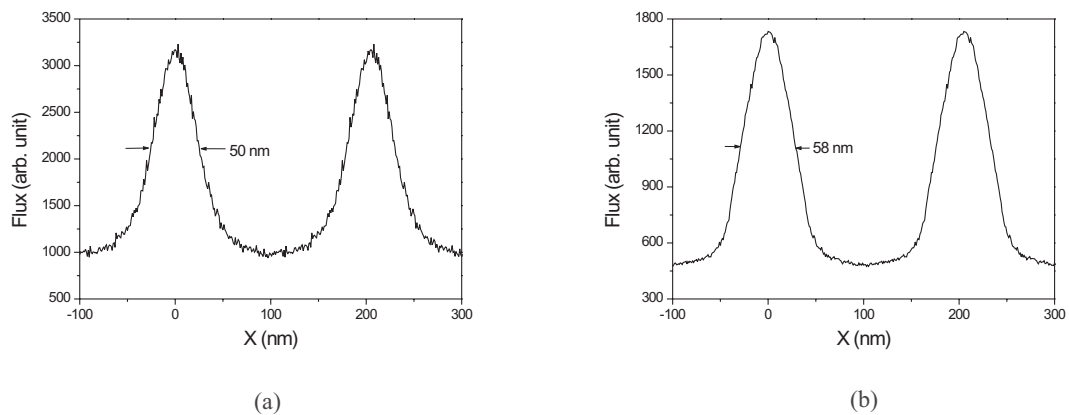


Figure 2.7: Atomic flux distribution at the focal plane (a) Atoms have a monochromatic longitudinal velocity of 565 m/s and a Gaussian distributed transverse spread of 28 cm/s (b) Atoms have a thermal Maxwell-Boltzmann distributed longitudinal velocity and a Gaussian distributed transverse spread of 28 cm/s. In the simulation, the laser beam used to generate the standing wave has a maximum saturation parameter of $s_0 = 75$ and its frequency is detuned relative to the $F = 4 \rightarrow 5$ transition at 410 nm by $\Delta = 5.7\Gamma$. The interaction length between the atoms and laser field is roughly $100 \mu\text{m}$.

Chapter 3

Apparatus

In this chapter we will have a discussion of the experimental set-up used for laser manipulation of indium atoms. The whole set-up is separated into two major parts: optical and vacuum part. The optical part includes the GaN diode lasers for 410 nm light and the frequency doubling of a Ti:Sapphire laser for 451 nm light. The vacuum part consists of the atomic oven and the vacuum chambers.

3.1 GaN diode laser

In 1997, Nichia Corporation achieved the first room temperature blue/violet GaN diode laser at 405 nm with cw operation for over 10,000 hours [23]. The output power was 5 mW. After several years of development the maximum output power has reached 50 mW. Within the scope of our experiment, we work with the DL100 diode laser system from Toptica which uses Nichia's 410 nm laser diode. It delivers an output power of 30 mW.

Typically, standard diode lasers have a linewidth of ten to several hundred MHz. For most applications this is sufficient, but for high resolution spectroscopy and some other applications such as laser cooling in our case, a much narrower linewidth is required to locate and resolve discrete atomic spectroscopic lines. One method is the application of an External Cavity Diode Laser (ECDL) in Littrow geometry (Figure 3.1). A diffraction grating is utilized to reflect the first order back into the laser diode, while the zeroth order is coupled out for experiments. The rear facet of the diode laser and the grating form an external cavity. In our case the linewidth is narrowed down to about 10 MHz. The wavelength of an ECDL can be tuned by changing the current and/or the temperature and/or tilting the diffraction grating. The laser wavelength is scanned by applying a scan voltage onto the piezo, with which the wavelength can be further fine-tuned. To have a large mode-hop free tuning range, a feed-forward current which is proportional to the

scan voltage is added onto the current. In this way, a mode-hop free tuning range of up to 20 GHz can be achieved for our laser systems. But the output power will change when this feed-forward is activated. With this ECDL configuration the output power of our lasers is 12 mW

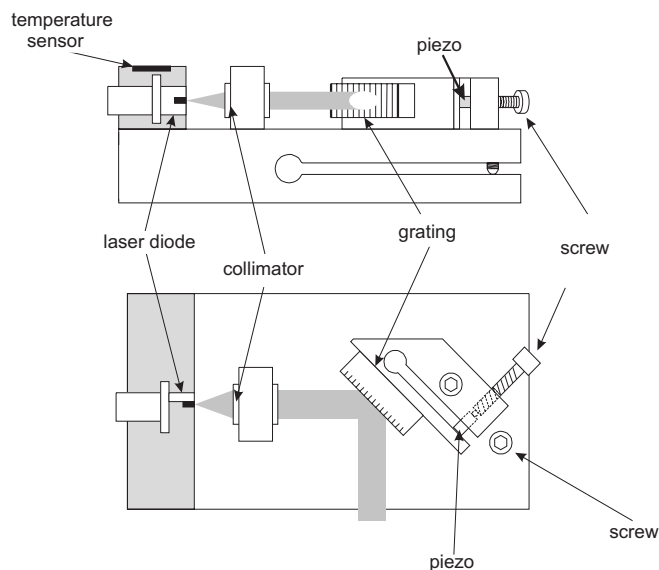


Figure 3.1: *Grating stabilized diode laser in side view (top) and top view (bottom)*

3.2 Frequency doubled Ti:Sapphire laser

3.2.1 Ti:Sapphire laser

The Ti:Sa laser which is used in our experiment (Model MBR-110) is a cw single frequency laser. The laser cavity is a bow-tie ring configuration together with an optical-diode to achieve single frequency operation. The wavelength can be tuned coarsely by a birefringent filter and finely by an intracavity thin etalon to achieve a maximum mode-hop free scan of 20 GHz. The frequency is locked onto a high finesse reference cavity using a fraction of the laser output. The laser linewidth was measured to be about a few hundreds of kHz.

The Ti:Sapphire laser is optically pumped by a 10 W frequency doubled Nd:YAG laser at 532 nm. We found that there is no lasing at 902 nm due to a water absorption line at this wavelength (see Figure 3.2). By purging the laser cavity with dry nitrogen, the output power can reach 900 mW.

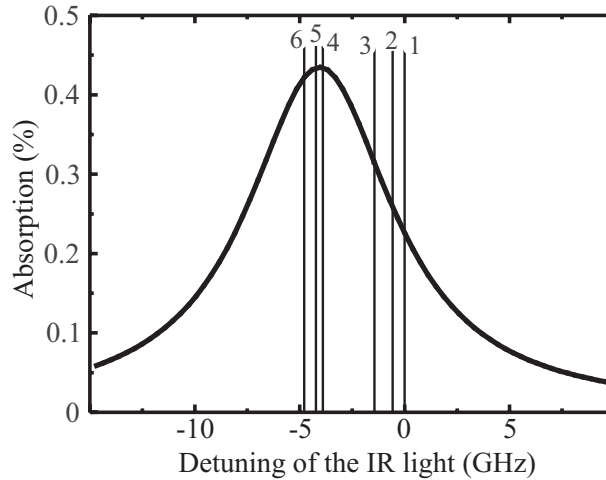


Figure 3.2: Water absorption line at 11083 cm^{-1} for a temperature of 298 K , a path length of 1 m , a total pressure of 1013 mbar and a H_2O partial pressure of 101.3 mbar [24]. The positions for the corresponding frequency doubled resonant radiation exciting the $(4, 5, 6) \rightarrow 5$ and $(3, 4, 5) \rightarrow 4$ transitions are labelled as 1, 2, 3 and 4, 5, 6, respectively.

3.2.2 Second harmonic generation (SHG)

A dielectric polarization $P(t)$ is induced when an electric field $E(t)$ travels through a medium, and can be represented by an infinite power series expansion [25, 26]

$$\begin{aligned} P(t) &= \epsilon_0 \chi^{(1)} E(t) + \epsilon_0 [\chi^{(2)} E^2(t) + \chi^{(3)} E^3(t) + \dots] \\ &= P_{lin}(t) + P_{nonlin}(t), \end{aligned} \quad (3.1)$$

where ϵ_0 is the electric permeability in vacuum and $\chi^{(n)}$ is the n th-order electric susceptibility. Second harmonic generation is related to the second-order electric susceptibility $\chi^{(2)}$. If we consider a monochromatic plane wave with an electric field

$$E(t) = E e^{-i\omega t} + c.c. \quad (3.2)$$

travelling through a medium with only second-order nonlinearity, the induced second-order nonlinear polarization can be written as

$$P^{(2)}(t) = \epsilon_0 \left[2\chi^{(2)} E E^* + \left(\chi^{(2)} E^2 e^{-i(2\omega)t} + c.c. \right) \right] = P_{dc}^{(2)} + P_{2\omega}^{(2)}. \quad (3.3)$$

The first term is a steady component and is called optical rectification, and the second one describes an electromagnetic wave with a frequency of 2ω .

The nonlinear susceptibility is usually a complex tensor. The second-order susceptibility is generally defined by the expression [26]

$$P_i^{(2)}(\omega_m + \omega_n) = \epsilon_0 \sum_{jk} \sum_{(nm)} \chi_{ijk}^{(2)}(\omega_m + \omega_n; \omega_m, \omega_n) E_j(\omega_m) E_k(\omega_n). \quad (3.4)$$

Here ω_m and ω_n are two frequency components. The indices ijk refer to the cartesian components of the fields. The notation (nm) indicates that, in performing the summation over n and m , the sum $\omega_m + \omega_n$ is to be held fixed. In the case of second harmonic generation, where $\omega = \omega_m = \omega_n$, expression (3.4) becomes

$$P_i^{(2)}(2\omega) = \epsilon_0 \sum_{jk} \chi_{ijk}^{(2)}(2\omega; \omega, \omega) E_j(\omega) E_k(\omega). \quad (3.5)$$

The second-order susceptibility is a third-rank tensor containing 27 components. It will vanish in a medium possessing inversion symmetry. For second harmonic generation, if the propagation and polarization directions of the fundamental and the second harmonic waves are known, a scalar effective nonlinear coefficient d_{eff} can be derived to describe the nonlinear polarization

$$P(2\omega) = \epsilon_0 d_{eff} E^2(\omega). \quad (3.6)$$

Reference [27] describes how d_{eff} can be calculated. In the case of linear polarized fundamental light of frequency ω , the second harmonic power $P_{2\omega}$ is expressed as [28]

$$\begin{aligned} P_{2\omega} &= \gamma_{SHG} P_\omega^2 \\ &= 2 \left(\frac{\mu_0}{\epsilon_0} \right)^{\frac{3}{2}} \frac{\omega^2 d_{eff}^2 l^2}{n_\omega^3} \frac{\sin^2(\Delta k l / 2)}{(\Delta k l / 2)^2} \frac{1}{A} \cdot P_\omega^2, \end{aligned} \quad (3.7)$$

where A is the cross section of the fundamental light beam, l is the length of the crystal, n_ω is the refractive index of the fundamental light, and Δk is the phase mismatching which is defined as

$$\Delta k = k_{2\omega} - 2k_\omega = \frac{2\omega}{c} (n_{2\omega} - n_\omega). \quad (3.8)$$

Here c is the speed of light, $n_{2\omega}$ is the refractive index of the second harmonic light, k_ω and $k_{2\omega}$ are the wave vectors of the fundamental and second-harmonic light, respectively.

3.2.3 Phase matching

According to Eq. (3.7), a prerequisite for efficient second harmonic generation is perfect phase matching $\Delta k = 0$, or using Eq. (3.8),

$$n_{2\omega} = n_\omega. \quad (3.9)$$

If $\Delta k \neq 0$, the second harmonic wave generated at one position is not in phase with the waves generated at other positions. This results in the interference described by

$$\frac{\sin^2(\Delta k l / 2)}{(\Delta k l / 2)^2}. \quad (3.10)$$

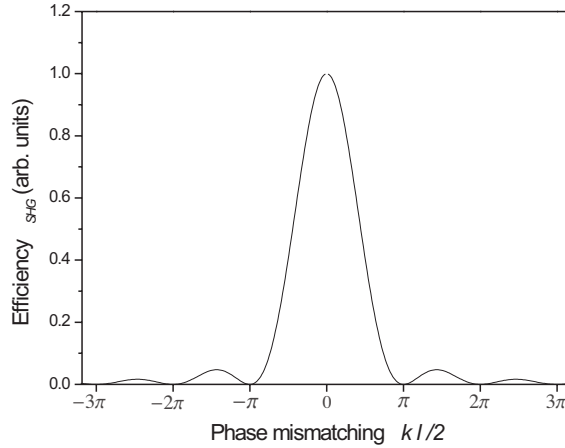


Figure 3.3: *Efficiency of the frequency-doubling dependent on the phase matching*

Because of normal dispersion, the phase matching is never fulfilled in isotropic crystals. The use of anomalous dispersion is almost impossible since it requires an absorption and thus detrimental resonance. The phase matching can be fulfilled in birefringent crystals in which the refractive index depends on the direction of polarization of the light wave. Typically, phase matching is achieved with two methods: angle tuning and temperature tuning. For angle tuning, an incident angle can be found along which the fundamental light has the same refractive index as that of the generated second harmonic light. For some crystals, e.g. KNbO_3 and LiNbO_3 , the birefringence depends strongly on the temperature. Then phase matching can be fulfilled by varying the temperature.

3.2.4 Lithiumtriborate (LBO)

Lithiumtriborat (LBO) was developed by the Fujian Institute of Research on the Structure of Matter in China in 1988 [29]. It is a negative biaxial crystal possessing two optic axes and three different refractive indices n_x , n_y and n_z ($n_x < n_y < n_z$)

LBO can be both angle and temperature phase matched. We use the angle phase matching in our experiments (see Figure 3.4). Both the fundamental and the second harmonic beams propagate in the xy principle plane. The fundamental light at 902 nm is polarized normally to this plane and has a constant refractive index of $n_z=1.609$, whereas the second harmonic light at 451 nm is polarized in this plane and its refractive index varies from $n_x=1.584$ to $n_y=1.613$. Under this situation, a negative biaxial crystal is similar to a negative uniaxial crystal. The phase matching angle ϕ_{PM} is calculated to be 22.6° , at which both the fundamental light and the second harmonic light have the same

refractive index of 1.609. The effective nonlinear coefficient at this phase matching angle is -0.905 pm/V .

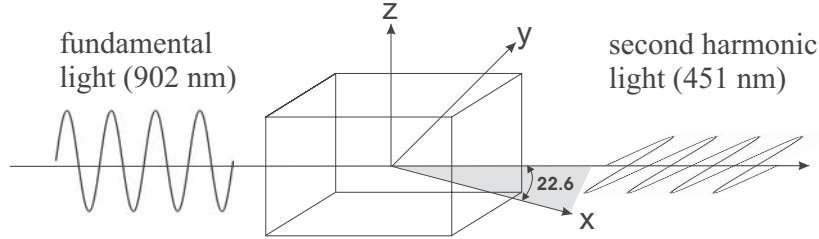


Figure 3.4: Scheme of frequency doubling with LBO crystal at 902 nm with a phase matching angle of 22.6° . x , y and z are the crystal axis, respectively. Both the fundamental and the second harmonic beams propagate in the xy principle plane. The polarization of the fundamental light is normal to xy plane and the one of the second harmonic light lies in xy plane

LBO has one disadvantage, i.e., it is sensitive to moisture, which will damage the crystal structure and reduce the nonlinearity. Thus, it is usually preserved and used in dry conditions [30]. Our frequency-doubling set-up is covered with a plastic box which is always purged with dry nitrogen. But even so, the degradation of the SHG performance can still not be avoided.

The LBO crystal used in our experiment has a size of $3 \times 3 \times 10 \text{ mm}^3$. To minimize the reflection of the linearly polarized fundamental light at the incident surface of the crystal, the crystal is cut such that the incident angle of the fundamental light whose polarization lies in the incident plane is the Brewster angle when the fundamental light propagates along the direction of the crystal edge in the crystal (see Figure 3.5).

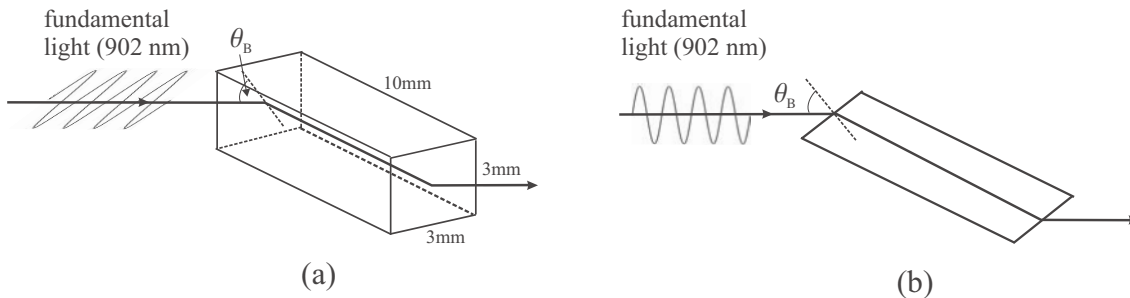


Figure 3.5: Scheme of the Brewster-cut LBO crystal for minimizing the reflection of the incident linearly polarized fundamental light at the incident surface of the crystal. The fundamental is polarized in the incident plane. θ_B is the incident angle in Brewster angle. (a) Three dimensional view and (b) The view from the top.

3.2.5 Boyd-Kleinman theory

In 1968, Boyd and Kleinman theoretically analyzed the frequency doubling with a Gaussian beam in the TEM_{00} mode [31]. In this case, the second harmonic power is expressed as [32]

$$\begin{aligned} P_{2\omega} &= \gamma_{SHG} P_{\omega}^2 \\ &= \frac{2}{\pi} \frac{\omega^3}{\varepsilon_0 c^4 n_{\omega}^2} d_{eff}^2 l P_{\omega}^2 h_m(B, \xi), \end{aligned} \quad (3.11)$$

where ω is the frequency of the fundamental light, l is the crystal length, ε_0 is the electric permeability in vacuum, c is the speed of light in vacuum, n_{ω} is the refractive index when phase matching is fulfilled. Here $h_m(B, \xi)$ is the correction factor which includes the focusing parameter ξ , defined as $\xi \equiv l/b$ for a confocal parameter $b \equiv 2\pi\omega_0^2/\lambda$, and the walk-off parameter B , defined as $B \equiv (\rho/2)\sqrt{lk_{\omega}}$ for a walk-off angle ρ . The subscript m in $h_m(B, \xi)$ indicates that the phase matching is achieved. Figure 3.6 shows curves of $h_m(B, \xi)$ for optimum phase matching as a function of ξ for several values of B .

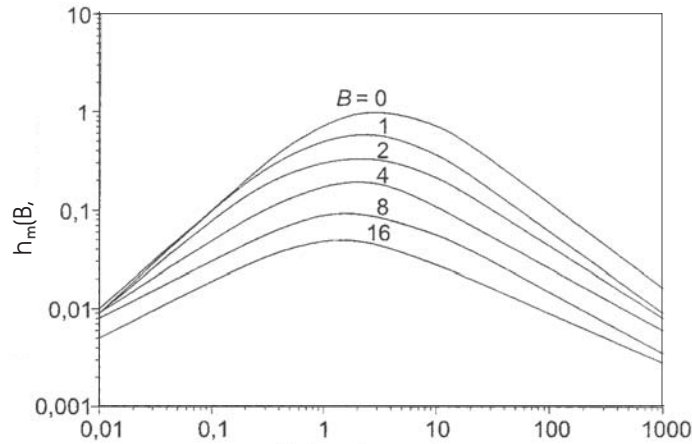


Figure 3.6: SHG power for optimum phase matching as a function of the focusing parameter ξ and the walk-off parameter B .

At the fundamental wavelength of 902 nm, with the known walk-off angle $\rho = 13.01$ mrad, the crystal length and the above derived refractive index, the walk-off parameter B is calculated to be

$$B = 2.177. \quad (3.12)$$

Consequently, the optimum focusing parameter and h_m can be obtained

$$\xi = 1.56 \quad (3.13)$$

$$h_m(2.177, 1.56) = 0.3 \quad (3.14)$$

Finally, the maximum conversion efficiency of the crystal is

$$\gamma_{SHG} = 7.6 \times 10^{-5} \text{ W}^{-1}. \quad (3.15)$$

From the above theory, an optimum focus for the frequency doubling with a Gaussian beam in the crystal can be derived

$$w_0 = \sqrt{\frac{l\lambda_\omega}{\xi 2\pi}}. \quad (3.16)$$

It is calculated to be $w_0 = 30.3 \mu\text{m}$ in our case.

3.2.6 Single-pass frequency doubling

To characterize the crystal, the conversion efficiency γ_{SHG} is measured. In the measurement the fundamental light single-passes through the crystal, and an interference filter is placed in front of the photodiode to filter out the fundamental light. This filter has a transmission of 90% at 451 nm which must be taken into consideration for the data analysis. Figure 3.7 shows the experimental result of frequency doubling in single-pass.

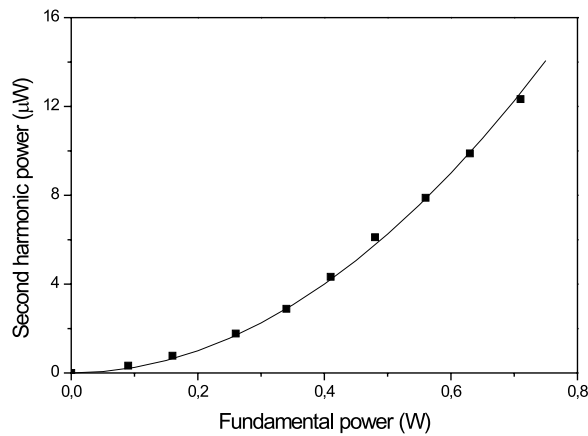


Figure 3.7: *Second harmonic power dependent on the incident fundamental power in single-pass experiment. The dots are experimental data and the solid curve is the fit based on the Eq. (3.11).*

By fitting the experiment data (see Eq. 3.11), the conversion efficiency is obtained

$$\gamma_{SHG} = 2.5 (\pm 0.1) \times 10^{-5} \text{ W}^{-1}. \quad (3.17)$$

This value is about 1/3 of the theoretically calculated maximum conversion efficiency (see Eq. (3.15)). The possible reasons could be the non-optimum focus in the crystal (see Eq. (3.16)) and the non-perfect crystal.

3.2.7 Resonator enhancement

From Eq. (3.7) we can see that the second harmonic power is proportional to the square of the fundamental power. In 1966, Ashkin *et al* discussed the enhancement of the second harmonic power by the enhancement of the fundamental power in an optical resonator [33]. The resonator used in our experiment is a bow-tie ring resonator consisting of two plane mirrors (M1 and M2) and two concave spherical mirrors (M3 and M4) with a curvature radius of 75 mm (Figure 3.8). M2 is mounted on a piezoelectric element used to scan and stabilize the resonator. The 902 nm fundamental light is coupled into the resonator through M1, and the generated 451 nm light is coupled out through M4. There are two waists in the resonator. One (w_{01}) locates in the center of the crystal, and another (w_{02}) lies between M1 and M2.

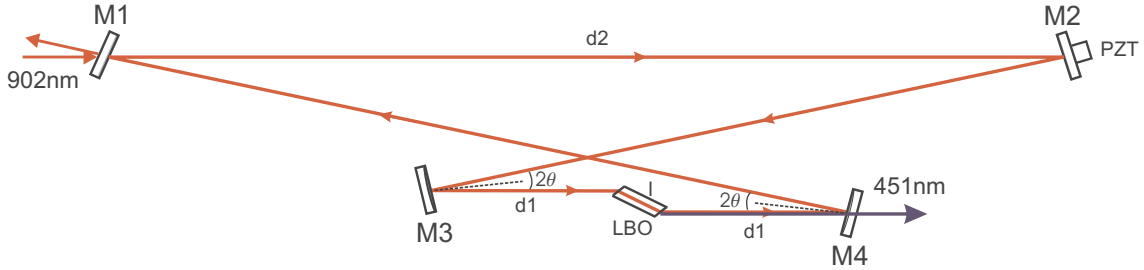


Figure 3.8: Schematic view of our bow-tie ring resonator with a Brewster-cut LBO crystal. M1 and M2: plane mirror, M3 and M4: concave spherical mirrors with a curvature radius of 75 mm, l : length of the crystal, $d1$: distance between the spherical mirror and the crystal surface, $d2$: the optical path starting from M4 through M1 and M2 to M3, PZT: piezoelectric element, θ : incident angle of the fundamental light onto the spherical mirror.

For a stable cavity, the phase must reproduce itself after one round trip. The stability of a resonator can be analyzed with the ABCD matrix formalism of the Gaussian beam [28]. Before the calculation of the stability, the astigmatism will be discussed first.

Astigmatism appears when the focus in the sagittal plane (normal to the resonator plane) does not overlap with the focus in the tangential plane (parallel to the resonator plane). In the resonator, the spherical mirror and the Brewster-cut crystal introduce astigmatic distortions.

For a spherical mirror, the focus in the sagittal plane has a different location than that in the tangential plane at oblique incidence [34]. This leads to two different focal lengths f_{tan} and f_{sag} for a spherical mirror with a curvature radius of r

$$f_{tan} = \frac{r}{2 \cos \theta} \quad f_{sag} = \frac{r}{2} \cos \theta, \quad (3.18)$$

where θ is the incident angle. The matrices for the curved mirror are accordingly

$$M_{tan}^m = \begin{pmatrix} 1 & 0 \\ -\frac{2}{r}\cos\theta & 1 \end{pmatrix} \quad M_{sag}^m = \begin{pmatrix} 1 & 0 \\ -\frac{2}{r}\frac{1}{\cos\theta} & 1 \end{pmatrix}. \quad (3.19)$$

A Brewster-cut crystal also acts differently on the light traversing in the sagittal and the tangential planes due to two different effective propagation lengths in the crystal [35]. The beam transfer matrices at the incident plane of the crystal are given by

$$M_{in,tan}^c = \begin{pmatrix} n & 0 \\ 0 & \frac{1}{n^2} \end{pmatrix} \quad M_{in,sag}^c = \begin{pmatrix} 1 & 0 \\ 0 & \frac{1}{n} \end{pmatrix}, \quad (3.20)$$

and at the exit plane are

$$M_{out,tan}^c = \begin{pmatrix} \frac{1}{n} & 0 \\ 0 & n^2 \end{pmatrix} \quad M_{out,sag}^c = \begin{pmatrix} 1 & 0 \\ 0 & n \end{pmatrix}. \quad (3.21)$$

The astigmatic distortions introduced by these two components can be compensated with each other to produce a maximum overlap of the stability ranges in the tangential and the sagittal plane. This compensation is achieved by varying the angle θ and the optical path $d2$ for a fixed curvature of the spherical mirrors.

Starting from the central plane of the crystal, the overall matrices in both the tangential plane and the sagittal plane are given by

$$M_{tan} = \begin{pmatrix} A & B \\ C & D \end{pmatrix}_{tan} = L M_{in,tan}^c D1 M_{tan}^m D2 M_{tan}^m D1 M_{out,tan}^c L \quad (3.22)$$

$$M_{sag} = \begin{pmatrix} A & B \\ C & D \end{pmatrix}_{sag} = L M_{in,sag}^c D1 M_{sag}^m D2 M_{sag}^m D1 M_{out,sag}^c L. \quad (3.23)$$

Here L, D1 and D2 are the propagation matrices, written as $\begin{pmatrix} 1 & l/2 \\ 0 & 1 \end{pmatrix}$, $\begin{pmatrix} 1 & d1 \\ 0 & 1 \end{pmatrix}$ and

$\begin{pmatrix} 1 & d2 \\ 0 & 1 \end{pmatrix}$, respectively. A resonator is stable only when $2 \leq A + D \leq 2$ [28]. Figure 3.9

shows the calculated stability diagram. The following cavity parameters are selected:

$$d1 = 38 \text{ mm} \quad (3.24)$$

$$d2 = 524 \text{ mm} \quad (3.25)$$

$$\theta = 6^\circ. \quad (3.26)$$

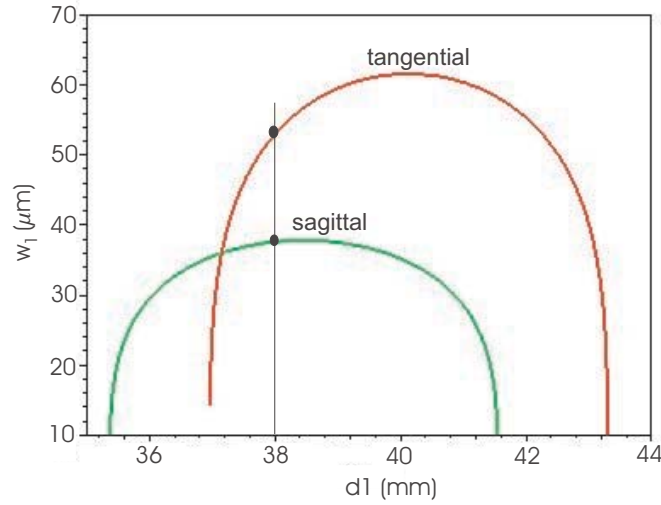


Figure 3.9: Stability diagram of the resonator with an angle of $\theta = 6^\circ$ and an optical path of $d_2=524$ mm. The black dots are the selected stability points in two planes which give the resonator geometry.

The corresponding waist sizes in the resonator are

$$w_{1,tan} = 53 \mu\text{m} \quad w_{1,sag} = 38 \mu\text{m} \quad (3.27)$$

$$w_{2,tan} = 341 \mu\text{m} \quad w_{1,sag} = 226 \mu\text{m} . \quad (3.28)$$

3.2.8 Mode matching

Once the geometry of the resonator is fixed, the mode parameters of the resonator is determined. To achieve the most efficient coupling of the fundamental beam into the resonator, the mode of the input fundamental laser beam must match the mode of the resonator as well as possible. This process is usually called mode matching. With the measured propagation parameters of the Ti:Sa laser and the calculated mode parameters of the resonator, the mode matching can be calculated by the ABCD matrix formalism. in our experiment, a pair of lenses with a focal length of 150 mm are utilized for the mode matching (see Figure 3.10).

3.2.9 Impedance matching and power enhancement

For a maximal enhancement of the fundamental power in the resonator, the impedance matching must be fulfilled. In analogy to the impedance matching in the high frequency technique to avoid the signal reflection at the end of a cable, the impedance matching for

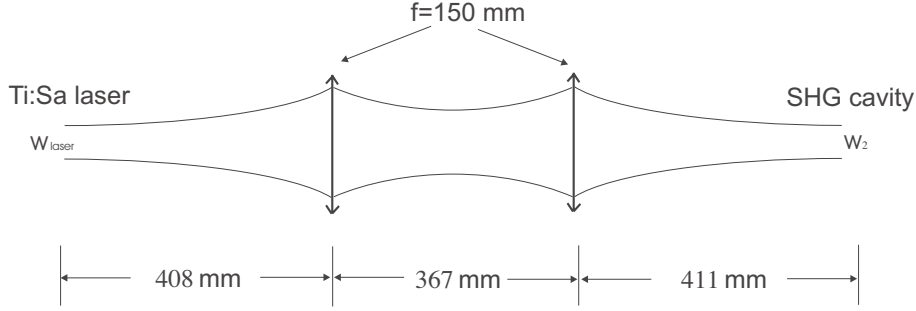


Figure 3.10: Mode matching between the Ti:Sa laser and the frequency-doubling cavity. w_{laser} and w_2 are the beam waists of the Ti:Sa laser and the above referred second waist in the frequency-doubling cavity, respectively.

the resonator means that the fundamental power is coupled into the resonator as much as possible and not reflected. To this end the transmission of the input mirror must match the losses in the resonator.

Since the losses in the resonator strongly depend on the input fundamental power, the optimum impedance matching with a certain transmission of the input mirror is different for the different input fundamental power. An analysis of impedance matching of an optical resonator has been done by Ashkin *et al* [33]. Let T_1 and R_1 be the transmission and the reflection of the input mirror $M1$

$$T_1 + R_1 = 1 . \quad (3.29)$$

Now define P_{in} , P_r and P_c as the incident power, the reflected power and the power inside the resonator incident on the crystal, respectively. When the resonator is on resonance, the power in the cavity and the reflected power are given by

$$\frac{P_c}{P_{in}} = \frac{T_1}{(1 - \sqrt{R_1 R_c})^2} \quad (3.30)$$

$$\frac{P_r}{P_{in}} = \frac{(\sqrt{R_1} - \sqrt{R_c})^2}{(1 - \sqrt{R_1 R_c})^2} . \quad (3.31)$$

Here R_c describes the reflection of the resonator which can be written as

$$R_c = R_m(1 - \gamma_{SHG}P_c) , \quad (3.32)$$

where R_m is the reflection describing the losses including the non-perfect reflection of the mirrors, the absorption of the crystal and other losses. The term $1 - \gamma_{SHG}P_c$ describes the loss of the fundamental light due to the second harmonic generation. Inserting Eq. (3.32) into Eq. (3.30) we obtain

$$\frac{P_c}{P_{in}} = \frac{T_1}{(1 - \sqrt{R_1 R_m(1 - \gamma_{SHG}P_c)})^2} , \quad (3.33)$$

from which the power circulating inside the resonator can be calculated.

If $R_1 = R_c$, then there is no reflected power from the resonator and the impedance matching is fulfilled. Under this situation, the power circulating in the resonator is

$$\frac{P_c}{P_{in}} = \frac{T_1}{(1 - \sqrt{R_1 R_c})^2} = \frac{1}{1 - R_c}. \quad (3.34)$$

Expression (3.33) tells us that the resonant enhancement is strongly dependent on the losses in the resonator.

To investigate the deviation of the transmission of an input mirror from the optimum transmission, a parameter σ is introduced

$$\sigma = \frac{1 - \sqrt{R_1}}{1 - \sqrt{R_c}}. \quad (3.35)$$

If the transmission of the input mirror and the losses in the resonator are very small, then

$$\sigma \approx \frac{1 - R_1}{1 - R_c} \quad (3.36)$$

$$\frac{P_c}{P_{cm}} = \frac{4\sigma}{(\sigma + 1)^2}, \quad (3.37)$$

where P_{cm} is the power in the resonator when it is impedance matched and on resonance. This relationship is plotted in Figure 3.11. It can be seen that there is still considerable enhancement even for a significant mismatch. When σ equals to 0.5 or 2, the enhancement reaches 90% of the maximum value.

3.2.10 Hänsch-Couillaud stabilization

The resonator continuously delivers the maximum power only when it is resonant at the fundamental wavelength. Thus, an error signal with sign change at resonance must be created to stabilize the resonator. The utilized stabilization method for our cavity was developed by Hänsch and Couillaud (see Figure 3.13) [36]. By this method a dispersive error signal is obtained. Its advantage over other methods [37, 38] is that no amplitude- or frequency-modulation is needed, so the broadening of the laser linewidth is avoided.

The electric amplitude $E^{(i)}$ of the input fundamental light can be decomposed into two components that are normal (s-polarized) and parallel (p-polarized) to the resonator plane, respectively:

$$E_p^{(i)} = E^{(i)} \cos \alpha \quad E_s^{(i)} = E^{(i)} \sin \alpha, \quad (3.38)$$

where α is the angle of the polarization of the linearly polarized fundamental light with respect to the normal plane. Because the LBO crystal is Brewster-cut (see chapter 3.2.4),

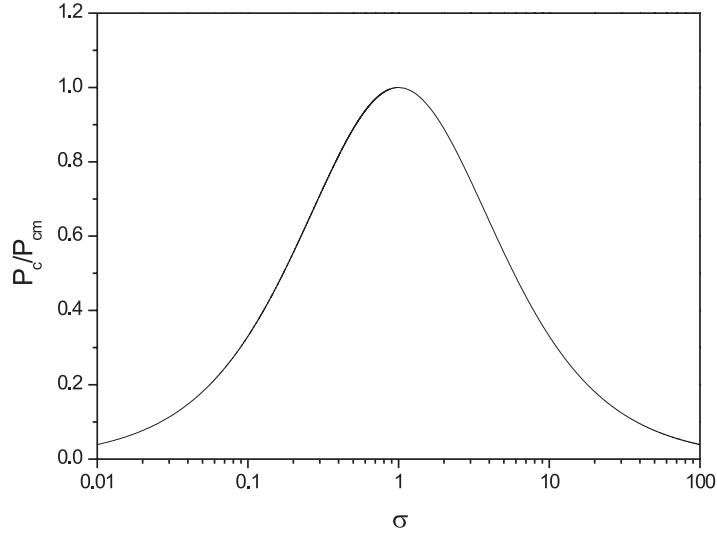


Figure 3.11: Power enhancement dependent on the mismatch parameter σ .

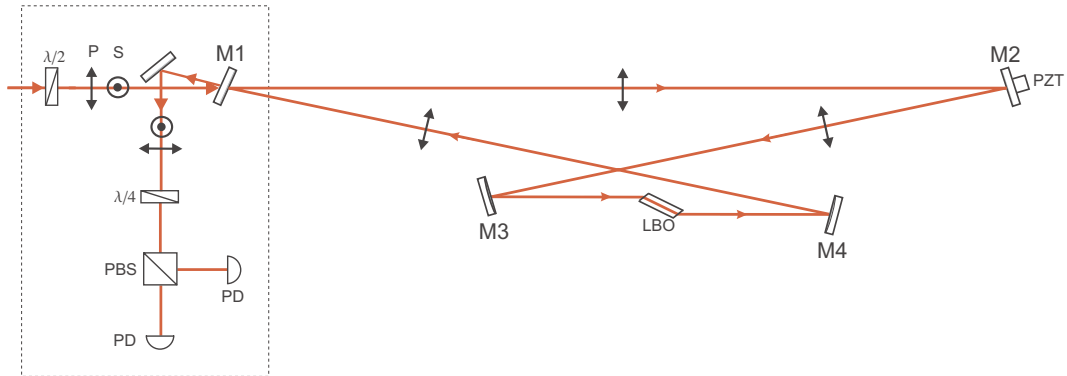


Figure 3.12: Schematic view of the Hänsch-Couillaud stabilization. Due to the Brewster-cut crystal (see chapter 3.2.4), only the p-polarized component of the fundamental light can circulate in the resonator, while the s-polarized component is reflected. P: p-polarization, S: s-polarization, $\lambda/2$: half-wave plate for 902 nm, $\lambda/4$: quarter-wave plate for 902 nm, PBS: polarizing beam splitter, PD: photodiode, .

only the p-polarized component of the fundamental light can circulate in the resonator and considerably be enhanced, while the s-polarized component is reflected by the resonator and used as a reference. This crystal is the necessary polarizing element for Hänsch-Couillaud stabilization. The reflected electric fields from the resonator are given by

$$E_p^{(r)} = E_p^{(i)} \frac{R_1 - R_c e^{i\delta}}{\sqrt{R_1}(1 - R_c e^{i\delta})} \quad (3.39)$$

and

$$E_s^{(r)} = E_s^{(i)} \sqrt{R_1}, \quad (3.40)$$

respectively. When the resonator is on resonance, there is no phase shift ($\delta = m \cdot 2\pi$) between $E_p^{(r)}$ and $E_s^{(r)}$. The sum of the two components is still linearly polarized. If the resonator deviates slightly off resonance, there exists a phase shift ($\delta \neq m \cdot 2\pi$) for $E_p^{(r)}$ with respect to $E_s^{(r)}$. This results in an elliptically polarized light. The reflected light beam from the resonator passes through a quarter-wave plate and a polarizing beam splitter (PBS). Two photo diodes detect the light power at the two ports of the PBS. The orientation of the quarter-wave plate is rotated so that both photodiodes measure the same power when the resonator is on resonance, and hence the difference signal is zero. For an elliptically polarized light when the resonator is off-resonance, the power at the two ports of the PBS are different. The difference signal of two photo diodes has a dispersive lineshape and is derived as:

$$\Delta I = I_1 - I_2 = 2I^{(i)} \cos \alpha \sin \alpha \frac{T_1 R_c \sin \delta}{(1 - R_c)^2 + 4R_c \sin^2(\delta/2)}. \quad (3.41)$$

In our set-up, signals from the two photo diodes are electronically subtracted (see Figure 3.13) and inserted to a servo amplifier (lockbox). The error signal generated by the lockbox is fed back onto the PZT mounted on M3 to actively stabilize the cavity on resonance.

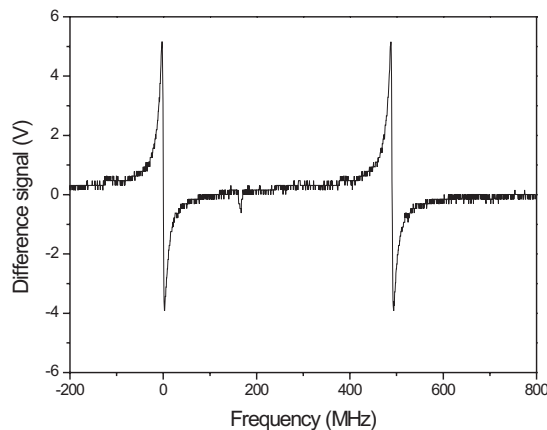


Figure 3.13: Experimentally recorded dispersive Hänsch-Couillaud error signal used for stabilizing the SHG resonator.

3.2.11 Performance of the SHG resonator

Figure 3.14 shows the fringes obtained by scanning the resonator with a linear ramp signal onto the PZT. It can be seen that 86 % of the incident fundamental light is coupled into the resonator in case of on resonance. The finesse of the resonator is measured to be 136.

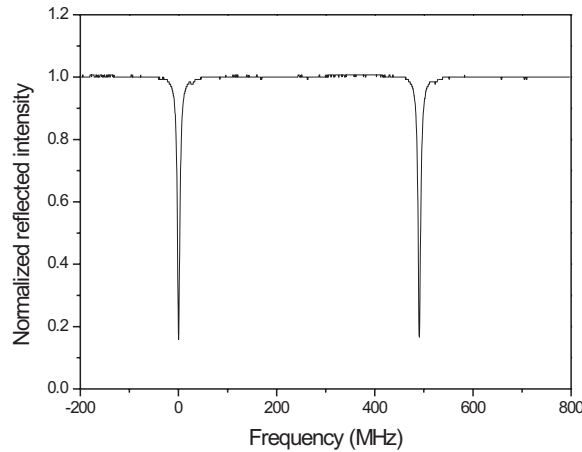


Figure 3.14: *Fringes obtained by observing the fundamental light reflected from the resonator when the resonator is scanned with a ramp signal.*

To extract the maximum second harmonic power from the resonator, a good impedance matching must be fulfilled. We have three input mirrors of different transmissions available ($T=0.75\%$, 1.5% and 3%). With a fundamental power of 800 mW , the SHG power with three different input mirrors are measured. They are normalized to the measured SHG power at $T=1.5\%$. The result is shown in Figure 3.15. During the measurement only the input mirror is realigned to achieve a maximum SHG power after each change. The solid curve in the graph is plotted according to the theory of impedance matching (see Eq. (3.35) and (3.36)) to show the normalized SHG power for different input mirrors. The optimum transmission lies between $T=0.75\%$ and $T=3\%$. Thus, the input mirror with a transmission of $T=1.5\%$ is the best one.

Figure 3.16 shows the dependence of the generated second harmonic power $P_{2\omega}$ on the fundamental power P_{ω} with the input mirror M1 of $T=1.5\%$. Theoretically, the circulating power inside the resonator P_c can be calculated using Eq. (3.33). The second harmonic power is given by

$$P_{2\omega} = \gamma_{\text{SHG}} \cdot P_c^2 . \quad (3.42)$$

With the measured single-pass conversion efficiency $\gamma_{\text{SHG}} = 2.5 \times 10^{-5} \text{ W}^{-1}$ and the

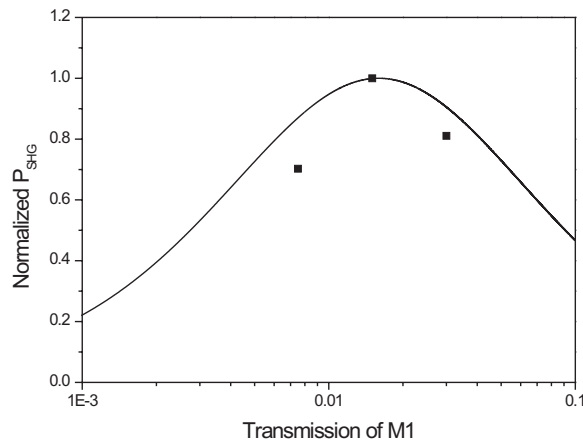


Figure 3.15: Impedance matching of the resonator. The square dots are the experimental data which are normalized to the measured SHG power at $T=1.5\%$, and the solid curve theoretically shows the change of the second harmonic power for different transmissions of $M1$.

reflection $R_m = 98.6\%$ (see Eq. (3.32)), $P_{2\omega}$ is calculated and plotted in Figure 3.16. We can see that the experimental result matches the theoretical calculation.

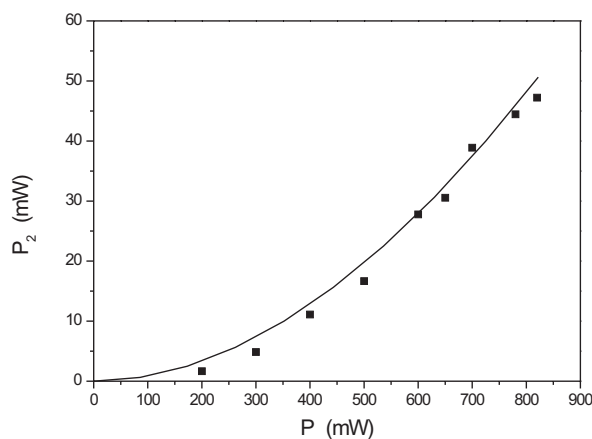


Figure 3.16: The dependence of the SHG power $P_{2\omega}$ on the fundamental power P_ω with the input coupler $M1$ of $T=1.5\%$. The square black dots are the measured data and the solid curve is plotted using Eq. (3.42).

3.3 Multi-frequency generation at 451 nm

As described in Chapter 2, five frequencies are needed for the laser manipulation experiments. For the two frequencies at 410 nm, we can use two diode lasers for each frequency, whereas the three frequencies at 451 nm can be generated with the following scheme (see Figure 3.17). First of all, the frequency of the blue light from the SHG cavity is set 318 MHz lower than the transition frequency of $5^2P_{3/2}(F = 5) \rightarrow 6^2S_{1/2}(F = 5)$. In other words, the laser frequency is 1435 MHz apart from the transition frequencies of $5^2P_{3/2}(F = 4) \rightarrow 6^2S_{1/2}(F = 5)$ and $5^2P_{3/2}(F = 6) \rightarrow 6^2S_{1/2}(F = 5)$, respectively. Then, the laser beam from the SHG cavity is split into two beams by a polarizing beam splitter (PBS) after passing through a half-wave plate. One beam travels through an Electro-Optical Modulator (EOM) which generates two sidebands, whose frequencies correspond to the transition frequencies of $5^2P_{3/2}(F = 4) \rightarrow 6^2S_{1/2}(F = 5)$ and $5^2P_{3/2}(F = 6) \rightarrow 6^2S_{1/2}(F = 5)$, respectively. Another beam is guided through an Acousto-Optical Modulator (AOM) which upshifts the laser frequency by 318 MHz to the transition frequency of $5^2P_{3/2}(F = 5) \rightarrow 6^2S_{1/2}(F = 5)$.

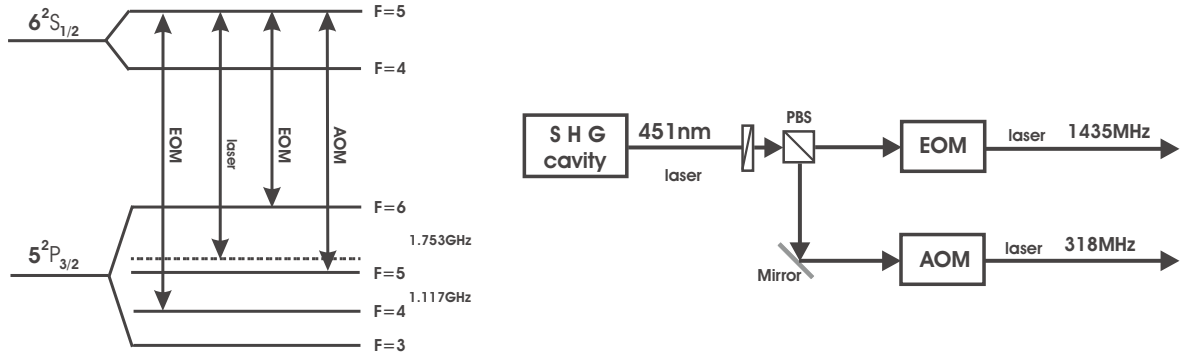


Figure 3.17: Scheme of the multi-frequency generation for light at 451 nm with an Electro-Optical Modulator (EOM) and an Acousto-Optical Modulator (AOM).

3.4 Vacuum system

The vacuum system for the atomic beam and laser cooling consists of the atomic oven and the chambers (see Figure 3.18). The atomic oven, which is normally used as a source for MBE process, can be heated to a temperature of 1200 °C to generate sufficient indium atomic flux. A turbo-molecular pump (Turbo-V 250, Varian) is connected to the lowest large chamber. The vacuum pressure can reach 10^{-8} Torr that is enough for the

experiments. Directly above the oven is a water-cooled copper shield with a large opening of a diameter of 5 mm in the center. It is used to remove most indium atoms from the vacuum. To reduce the divergence of the atomic beam, an aperture with an opening of a diameter of 0.5 mm in the center is mounted. The second chamber downstream is for laser cooling. It is a six-way cross (CF63) with 4 viewports AR-coated for both 410 nm and 451 nm light. After that there is a long drift tube used for a better detection of the laser cooling. A small chamber (CF35) is connected directly to this tube. A vacuum gauge is screwed on it to measure the vacuum pressure. On the top there is another small chamber (CF35) used for the detection and analysis of the signal of laser cooling.

The diameter of the atomic beam is measured to be about 1 mm in the cooling region and 5 mm in the probe region, leading to a full divergence of 6 mrad.

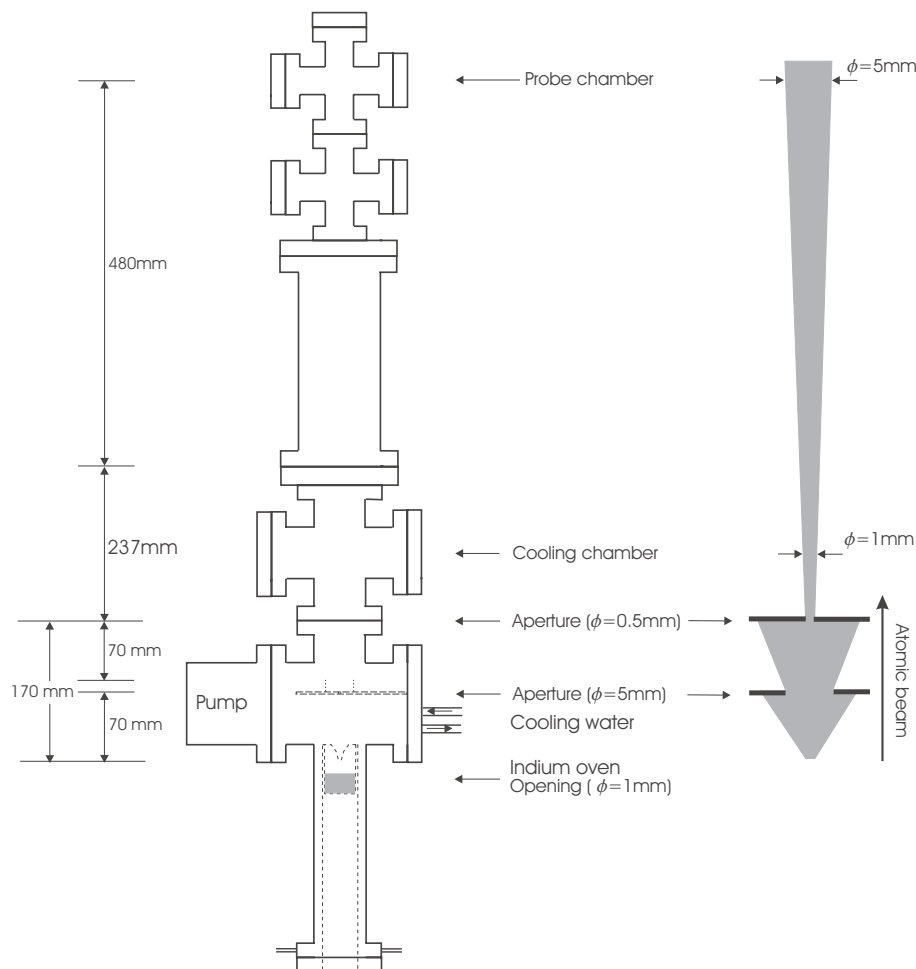


Figure 3.18: Schematic view of the vacuum system with the dimensions and the geometry of the atomic beam.

Chapter 4

Spectroscopy and frequency stabilization

In this chapter we will discuss the spectroscopic experiments performed with indium vapor and how the laser frequency can actively be stabilized onto an atomic transition frequency with the spectroscopic signals.

4.1 Atomic sources

Since the vapor pressure of indium is in the range of 10^{-34} Torr at room temperature, a suitable atomic spectroscopy cell is needed to generate sufficient atomic density for practical applications. To this end, a hollow cathode and an all-sapphire cell have been studied.

4.1.1 Hollow cathode

In the experiments we use a see-through type hollow cathode from Cathodeon (see Figure 4.1). It consists of a glass cell filled with 8 mbar of neon. Inside the cell there are two anodes and one hollow cathode which is made of InP. By applying a discharge current of 8-10 mA, indium is sputtered out of the cathode. The power supply has a modulation function which allows one to modulate the discharge current with a frequency of up to 500 Hz, and hence a phase-sensitive detection of the transmission signal with a lock-in amplifier is possible.

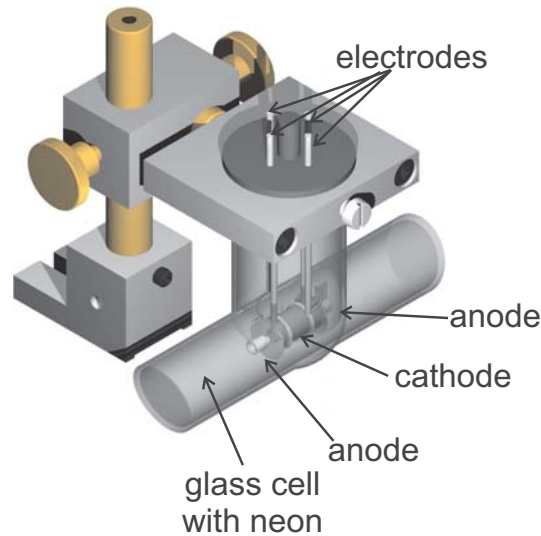


Figure 4.1: *Drawing of the hollow cathode used in the experiment.*

4.1.2 All sapphire cell

As an alternative to the hollow cathode, an all-sapphire cell is used as an atomic source (see Figure 4.2). It was developed and manufactured by the Institute for Physical Research in Armenia. The cell consists of a 107 mm long cylindrical sapphire tube with an inner diameter of 11 mm. At each end, a sapphire window is glued. Inside the cell 10 mg of pure indium is sealed. Two heating wires, made of NiCr, are wrapped around the cell with counter-propagating currents. Typically, with a current of 5 A, the cell can be heated to a temperature of 630 °C. At this temperature, about 94% atoms populate the $5^2P_{1/2}$ state and 6% the $5^2P_{3/2}$ state.

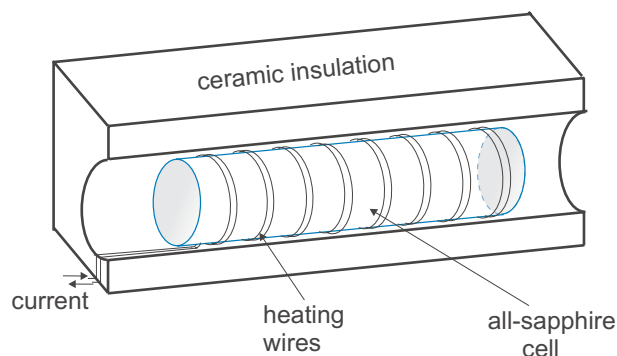


Figure 4.2: *Schematic view of the all sapphire cell and the oven (half).*

4.2 Absorption spectroscopy

The set-up of absorption spectroscopy on the hollow cathode is sketched in Figure 4.3. In the experiments, the current to the hollow cathode is switched on and off at a frequency of 500 Hz, and the transmission signal is demodulated with a lock-in amplifier. Figure 4.4 shows the absorption spectra of 410 nm and 451 nm light on the hollow cathode. Notice that the diode laser is scanned by applying a scan voltage onto the piezo (see chapter 3.1), and we transform the scan time to the frequency by assuming that the piezo reacts linearly to the applied scan voltage, but actually this reaction is not really linear.

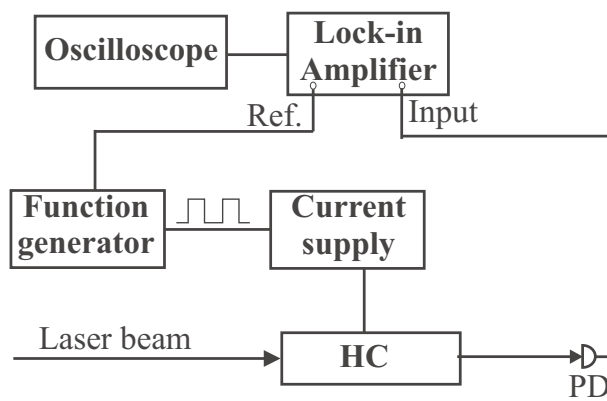


Figure 4.3: *Experimental set-up of the absorption spectroscopy on the hollow cathode. HC: hollow cathode; PD: photodiode.*

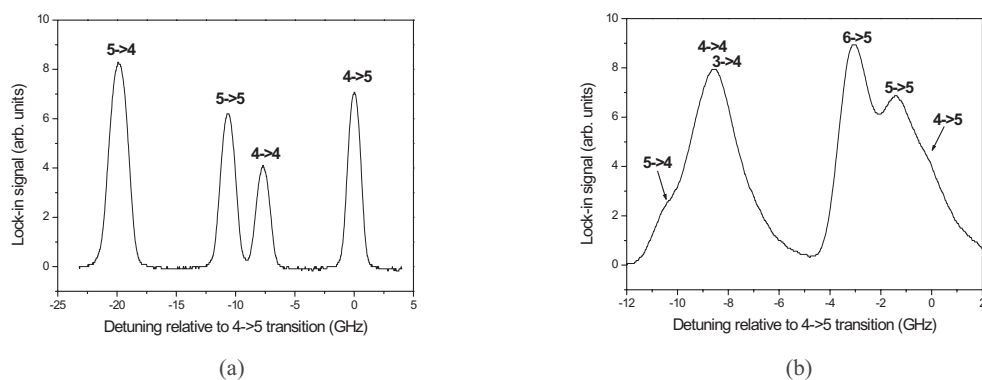


Figure 4.4: *Absorption spectra on the hollow cathode with (a) 410 nm light and (b) 451 nm light. The signals are obtained with phase-sensitive detection of the absorption signals.*

Due to the Doppler effect, the linewidth is about 1 GHz. For the $5^2P_{1/2} \rightarrow 6^2S_{1/2}$

transition, the hyperfine energy splitting of both $5^2P_{1/2}$ and $6^2S_{1/2}$ states are larger than 1 GHz, all four peaks are well resolved (see Figure 4.4 (a)). But for the $5^2P_{3/2} \rightarrow 6^2S_{1/2}$ transition, due to the small hyperfine energy splitting of the $5^2P_{3/2}$ state, the spectrum cannot be resolved (see Figure 4.4 (b)). It is noticed that, in the spectrum of 410 nm light, the relative signal strengths of 4 peaks ($4 \rightarrow 5$, $4 \rightarrow 4$, $5 \rightarrow 5$ and $5 \rightarrow 4$) are 87:50:76:100, which are different from the theoretical calculations 100:36:67:100. This could result from the feed-forward applied to the diode laser current which extends the scan range, but gives rise to a higher laser power at long wavelengths than at short ones.

To compare the signals obtained on the hollow cathode and the sapphire cell, we perform the experiments with 410 nm light (see Figure 4.5). In the experiments, the hollow cathode is operated with the maximum discharge current of 10 mA and the sapphire cell is heated to 630 °C. No phase-sensitive detections are used for the experiments. A comparative plot of the transmission spectra on the sapphire cell and the hollow cathode is shown in Figure 4.6. The absorption in the sapphire cell is obviously much stronger than in the hollow cathode.



Figure 4.5: *Experimental setup of absorption spectroscopy with 410 nm light on the hollow cathode (HC) and the all-sapphire cell (ASC), respectively. In the experiments, the discharge current of the hollow cathode is 10 mA and the temperature of the sapphire cell is 630 °C.*

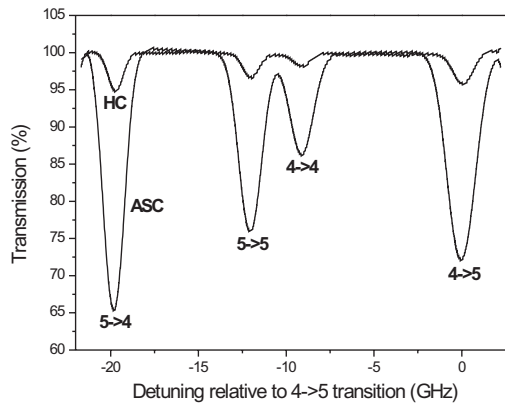


Figure 4.6: *Transmission spectra of 410 nm light for the hollow cathode (HC) and for the all-sapphire cell (ASC), respectively, for the same incident power of 30 μ W.*

We measure the width (FWHM) of the transmission peak ($4 \rightarrow 5$ transition at 410 nm) on the sapphire cell by fitting with a Gaussian line profile for the Doppler broadening (see Figure 4.7). The measured width is 1.5 GHz which is larger than the theoretical 1.36 GHz at 630 °C [40]. Since the width is proportional to the \sqrt{T} (T is the temperature in Kelvin) and hence not so sensitive to the cell temperature, the possible reason is, as mentioned above, that the piezo does not linearly react to the applied scan voltage.

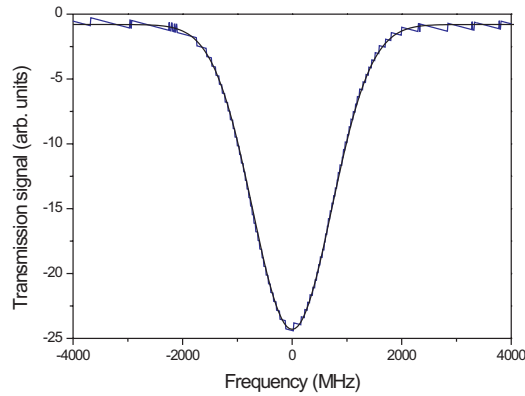


Figure 4.7: *Transmission profile of $4 \rightarrow 5$ transition at 410 nm on the sapphire cell. The smooth curve is the fit with a Gaussian line profile for the Doppler broadening.*

4.3 Saturation spectroscopy

To obtain narrow linewidths, saturation spectroscopy is applied (see Figure 4.8). It was first introduced by P. W. Smith and T. W. Hänsch in 1971 [41]. A small fraction of the laser beam from the diode laser is coupled out by a beam splitter. This beam is collimated and split into a strong pump beam ($P_{\text{pump}} = 70 \mu\text{W}$) and a weak probe beam ($P_{\text{pump}} = 30 \mu\text{W}$). The two beams propagate through the sapphire cell in opposite directions. The transmission signal of the probe beam is detected. Figure 4.9 (a) shows the transmission signal of the probe beam. In the center of each Doppler broadened peak, there is a so-called Lamb-dip signal [40]. Figure 4.9 (b) shows the peak of the $4 \rightarrow 5$ transition for an intense pump power of about 10 mW. Due to the strong depopulation pumping, a Lamb-dip with a contrast of 40 % is obtained.

In order to remove the Doppler-background, the pump beam is chopped at a frequency of 1.8 kHz and the transmission signal is demodulated with a lock-in amplifier. The output signal from the lock-in amplifier is shown in Figure 4.10.

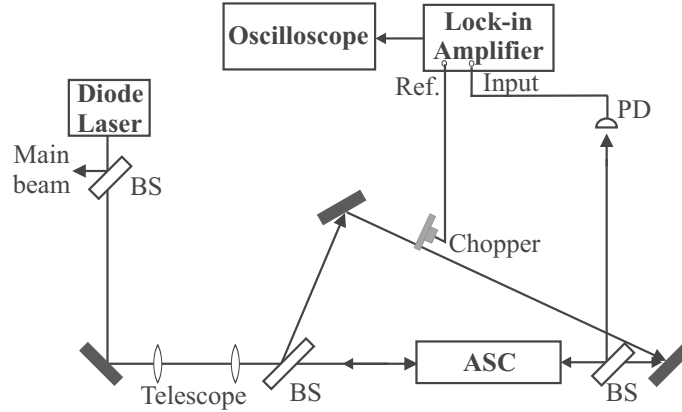


Figure 4.8: *Experimental setup of the saturation spectroscopy on the all sapphire cell (ASC). BS: beam splitter, PD: photodiode.*

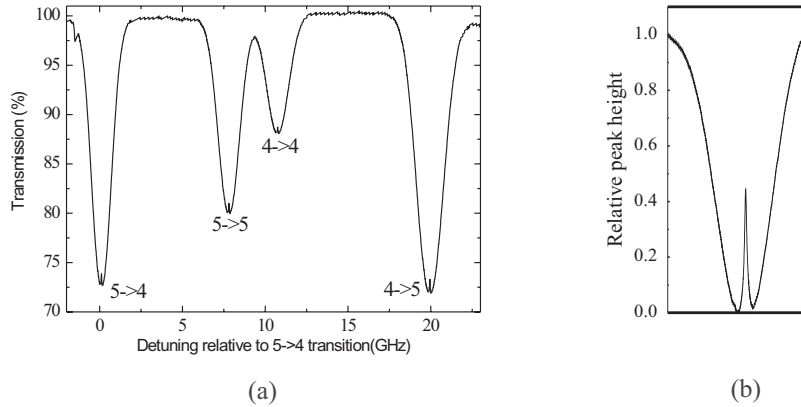


Figure 4.9: *Transmission signal obtained by saturation spectroscopy on the sapphire cell with 410 nm light. (a) Lamb-dip signals with Doppler background. (b) Zoom-in of the 4→5 peak for a pump power of about 10 mW.*

For a typical pump power of $70 \mu\text{W}$ used for frequency stabilization, the measured linewidth (FWHM) is about 50 MHz, which is larger than the natural linewidth of 25 MHz (see Eq. (2.3)). This is due to power broadening, a spectral laser linewidth of 10 MHz and a non-perfect alignment of the two counterpropagating beams.

We also tried to find the Lamb-dip signals with the hollow cathode, but no signal could be observed even with the help of a lock-in amplifier. It could be due to a large collision rate of the indium atoms with the buffer gas and electrons, which significantly reduces the depopulation of the ground states by the pumping beam.

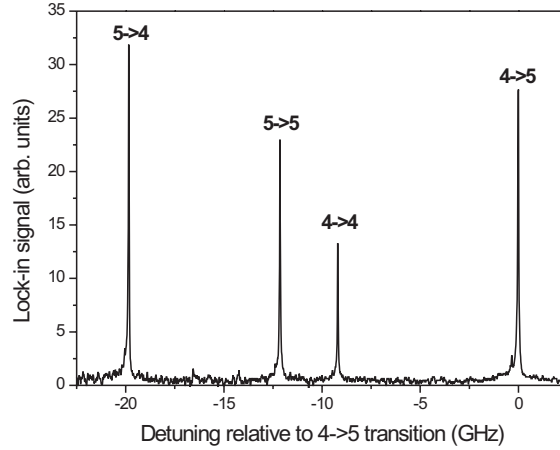


Figure 4.10: *Pure Lamb-dip signals of the saturation spectroscopy on the sapphire cell with 410 nm light.*

4.4 Polarization spectroscopy

Polarization spectroscopy is another method to get sub-Doppler linewidths [40, 42, 43]. The experimental set-up is sketched in Figure 4.11. The incident linearly polarized laser beam is collimated and split into a weak linearly polarized probe beam and a strong circularly polarized pump beam. The beams pass through the sapphire cell in opposite directions. The polarization plane of the probe beam is at an angle of 45° with respect to the polarizing beam splitter (PBS).

In the presence of the circularly polarized pump beam, due to the induced circular birefringence of the indium vapor originating from the nonuniform population distribution of the magnetic sublevels of the ground states by optical pumping, the polarization plane of the linearly polarized probe beam is rotated when it transverses the sapphire cell. This rotation is analyzed by measuring the intensities at the two ports of the PBS with two photodiodes (PD1 and PD2). The difference signal of two photodiodes has a dispersive line shape [44]. Figure 4.12 (a) shows the difference signals of PD1 and PD2 when the pump light is on and off. The background in the graph is found to result mainly from the linear Faraday effect which is a magnetic field induced circular birefringence rotating the linear polarization of the probe beam [45, 46].

Since the linear Faraday effect does not depend on optical pumping, this background can be removed by amplitude modulating the pump beam with a chopper and demodulating the difference signal by a lock-in amplifier. The signal is shown in Figure 4.12 (b).

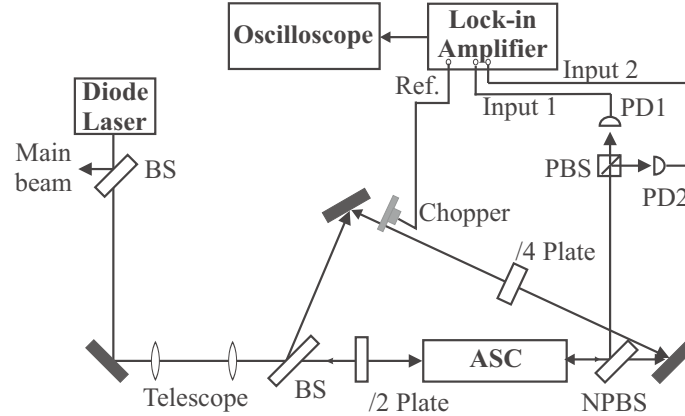


Figure 4.11: The experimental set-up of the polarization spectroscopy on the all sapphire cell (ASC). BS: beam splitter, PBS: polarizing beam splitter, NPBS: non-polarizing beam splitter PD1/PD2: photodiodes.

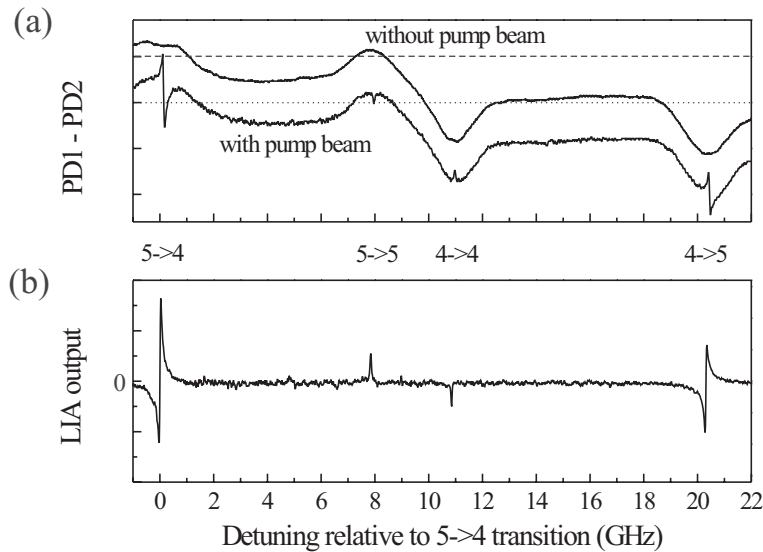


Figure 4.12: Signals of the polarization spectroscopy on the sapphire cell. (a) Differential signals of the two photodiodes with and without the pump beam. The corresponding zero-levels are indicated by the dotted and dashed line, respectively. (b) Demodulated signal from the Lock-in amplifier (LIA).

From the plot we find that the $5 \rightarrow 5$ and $4 \rightarrow 4$ transitions show a Lorentzian absorptive line shape instead of a dispersive one. This is due to the nonlinear Faraday effect

induced by the elliptically polarized pump beam, which rotates the linear polarization of the probe beam [46, 47]. This elliptically polarized pump beam arises from the initially circularly polarized pump beam after transversing through the non-polarizing beam splitter (NPBS). The main axis of this ellipse is at 20° with respect to the horizontal plane. The magnetic unshielded all-sapphire cell together with an elliptically polarized pump beam leads to an important contribution of this nonlinear Faraday effect in the sub-Doppler lines.

4.5 Fluorescence spectroscopy

The experimental set-up of the fluorescence spectroscopy is shown in Figure 4.13. A laser beam travels at right angle to the atomic beam and excites the atoms. We use a collecting optics consisting of two lenses to collect the emitted fluorescence. Between two lenses there is an interference filter which has a small spectral window (full width at half maximum transmission) of 13.4 nm at the transmission wavelength. Thus, the filter for 410 nm filters out nearly all 451 nm light, and vice versa. The fluorescence signal is detected by a photomultiplier. In the experiments, we excite the atoms with 410 nm light and detect the fluorescence signal at 451 nm, and vice versa. The spectra are shown in Figure 4.14.

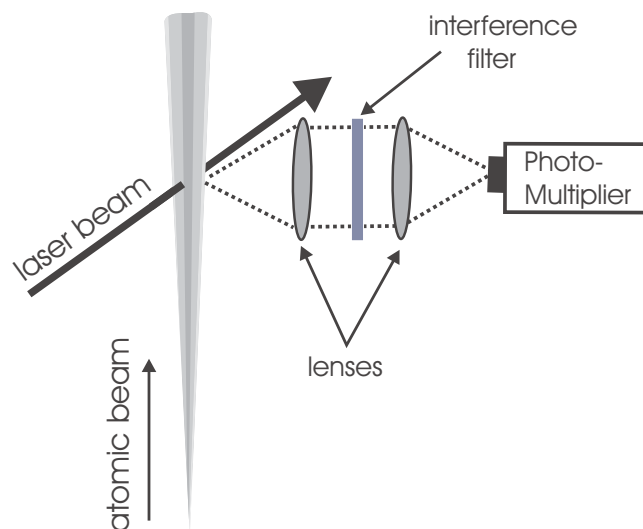


Figure 4.13: *The experimental set-up of the fluorescence spectroscopy on the atomic beam.*

In addition, we apply this spectroscopic method to check whether three necessary frequency components of the 451 nm light for laser manipulation experiments are generated

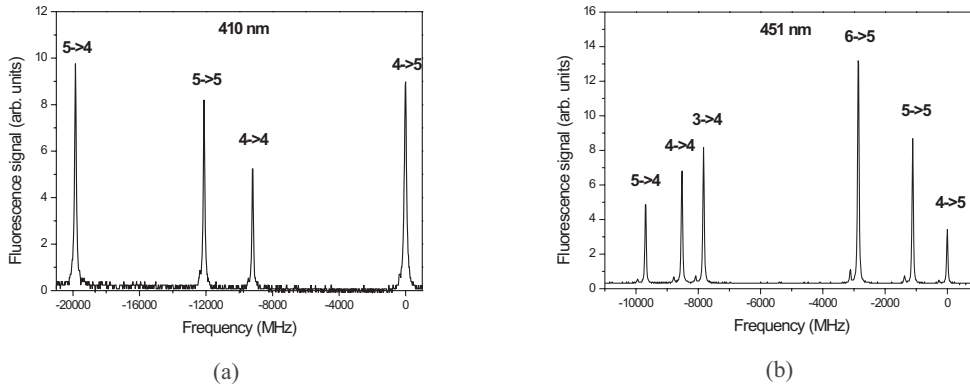


Figure 4.14: Fluorescence spectra on the atomic beam with (a) 410 nm excitation light and (b) 451 nm excitation light.

by the EOM and the AOM in the desired way (see chapter 3.1.3). In the experiment, two beams from the EOM and AOM are combined with a polarizing beam splitter before they hit the atomic beam. The spectrum shows a large peak generated when three frequency components excite the three transitions at 451 nm simultaneously (see Figure 4.15). This peak becomes smaller if either the EOM or the AOM is turned off, which indicates that all necessary frequency components are correctly generated. We have optimized the modulation frequencies of the EOM and AOM by maximizing the peak height.

4.6 Frequency stabilization

4.6.1 Allan variance

The frequency stability of a system can be characterized by analyzing the error signal in terms of the Allan variance [48]. For a finite measurement time, it is expressed as

$$\sigma_y^2 \approx \frac{1}{m} \sum_{k=1}^{m-1} \frac{(\bar{y}_{k+1} - \bar{y}_k)^2}{2}, \quad (4.1)$$

where \bar{y}_k is the average value of the frequency fluctuation in time interval $[t_k, t_{k+\tau}]$, which is written as

$$\bar{y}_k \equiv \frac{1}{\tau} \int_{t_k}^{t_k+\tau} y(t) dt. \quad (4.2)$$

It has been found that most frequency instabilities can be modelled by a combination of power-law noises having an Allan variance of the form $\sigma_y(\tau) \propto \tau^\alpha$. Thus, from the plot

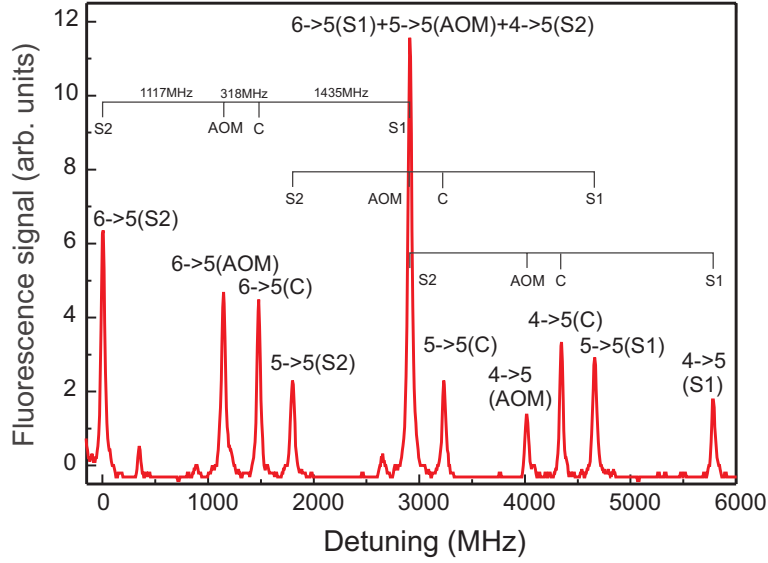


Figure 4.15: Fluorescence spectrum with 451 nm excitation light when the Electro-Optical modulator (EOM) and the Acousto-Optical modulator (AOM) are switched on. C: laser frequency from the SHG cavity, S1 and S2: two sideband frequencies generated by the EOM, AOM: the frequency upshifted by the AOM.

of the Allan variance $\sigma_y(\tau)$ against τ , the types of the noise can be obtained. Table 4.1 summarizes the five most often encountered noise types.

noise type	Allan variance $\sigma_y(\tau)$
Random Walk of the frequency	$\sigma_y(\tau) \propto \tau^{1/2}$
Flicker noise of the frequency	$\sigma_y(\tau) \equiv \text{constant}$
White noise of the frequency	$\sigma_y(\tau) \propto \tau^{-1/2}$
Flicker noise of the phase	$\sigma_y(\tau) \propto \tau^{-1} \cdot (\text{constant} + \ln \tau)^{1/2}$
White noise of the phase	$\sigma_y(\tau) \propto \tau^{-1}$

Table 4.1: Description of the noise types in terms of Allan variance.

4.6.2 Frequency stabilization of the diode lasers

To stabilize the frequency of the diode lasers at 410 nm, we can use either the Lamb-dip signal of the saturation spectroscopy or the dispersive signal of the polarization spectroscopy for the $4 \rightarrow 5$ transition, and the Lamb-dip signal of the saturation spectroscopy

for the $5 \rightarrow 5$ transition. The laser frequency is detuned from the atomic resonance frequency if it is locked on the slope of the Lamb-dip signal, whereas the laser frequency can be locked on the atomic resonant frequency by using the dispersive signal of the polarization spectroscopy. The advantage of such locking schemes is to avoid the frequency modulation and the associated spectral broadening of the laser light.

It is possible to lock the laser frequency on the atomic resonant frequency by using the Lamb-dip signal if the frequency modulation of the diode laser current instead of the amplitude modulation of the pump beam is used, through which a dispersive lineshape of the Lamb-dip signal can be obtained. However, this locking scheme introduces a broadening of the laser linewidth.

The output signal from the lock-in amplifier is inserted into a servo amplifier (SA) and subtracted by an adjustable DC offset to allow us to change the lock point. The output signal from the SA is fed back to the diode laser system to steer the position of the grating and hence the emission frequency.

In the experiments, we lock the laser frequency on the slope of the Lamb-dip signal of the saturation spectroscopy and the dispersive signal of the polarization spectroscopy, respectively. The characterization of the frequency stability is analyzed in terms of Allan variance (see Figure 4.16). In both cases, the locked laser shows a much smaller frequency fluctuation than the free-running laser. The stability is better than 200 kHz for integration times of 1-10 seconds. From the figures, it is observed that the white noise has an dominant influence on the frequency stability because it drops as $\tau^{-1/2}$. With both signals, the laser remains locked for more than one hour, which is sufficient for our experiments.

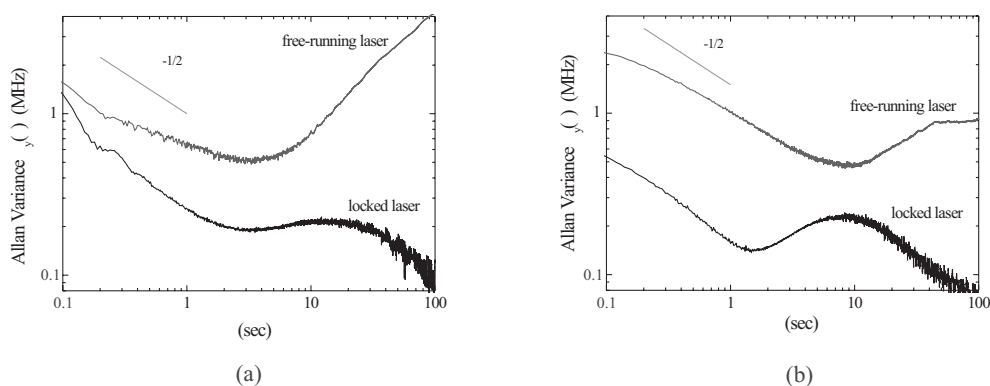


Figure 4.16: Allan variance $\sigma_y(\tau)$ of the error signal of a free-running laser and a laser locked on (a) the slope of the Lamb-dip signal of the saturation spectroscopy and (b) the dispersive signal of the polarization spectroscopy ($4 \rightarrow 5$ transition). The total data acquisition time was 70 minutes.

4.7 Two color spectroscopy

The generation of a suitable error signal for stabilizing the 451 nm laser on the atomic transition frequency is not that easy because the thermal population of the $5^2P_{3/2}$ state is only 6% at 630 °C. Thus, an optical pumping with the 410 nm laser becomes extremely important. The experimental set-up is sketched in Figure 4.17. A small fraction of the 410 nm diode laser beam is split into two beams. One beam is used to lock the frequency of the diode laser on the $4 \rightarrow 5$ transition with the above discussed frequency modulation method in the saturation spectroscopy (PD1). Another beam is used as the pump beam ($s_0^{410}=0.7$) and combined with the 451 nm light beam ($s_0^{451}=0.2$). Both beams have the same diameter of 1 mm and copropagate through the sapphire cell. In front of PD2 there is an interference filter used to block the 410 nm pump light. To remove the Doppler background the 410 nm pump beam is amplitude modulated with a chopper and the transmission signal is demodulated with a lock-in amplifier (LIA).

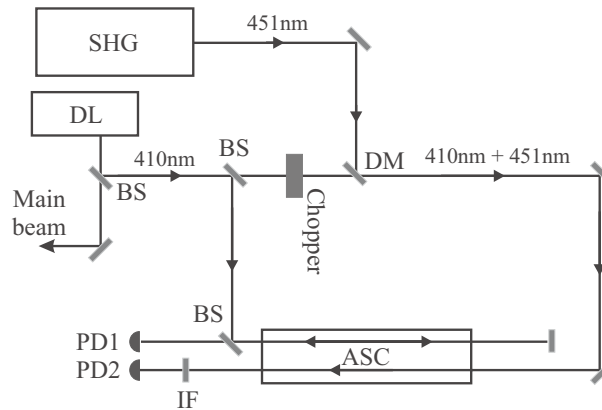


Figure 4.17: Set-up of the two color spectroscopy on the all-sapphire cell (ASC). SHG: frequency doubling cavity, DL: diode laser, BS: beam splitter, DM: dichroic mirror, IF: interference filter ($T@451\text{ nm}$), PD1/PD2: photodiodes.

Figure 4.18 shows the output signal of the lock-in amplifier when the 451 nm laser scans across the $5^2P_{3/2}$ ($F = 4, 5, 6$) \rightarrow $6^2S_{1/2}$ ($F = 5$) transitions. The spectrum shows unexpectedly broad peaks with a FWHM of an order several hundreds of MHz, which lies between the natural linewidth (25 MHz) and the Doppler width (1.5 GHz). Additionally, a dip is observed at the center of each peak for all transitions. The wide lineshape is neither Lorentzian nor Gaussian. We find that this peculiar lineshape is a combination of a Gaussian and a Lorentzian profile with FWHM of about 680 MHz and 190 MHz, respectively. Both linewidths exceed the breadth expected for a narrow velocity class probed in linear absorption spectroscopy at the level of 30-50 MHz. This enhanced linewidth may be attributed to the velocity changing collisions (VCC) which have been intensively studied

between atoms and perturbers (typically inert-gas atoms) at pressures of several hundred to 1000 mTorr [49, 50]. In our case, In-In ground state collisions, light induced collisions [51] and residual gas collisions could be considered.

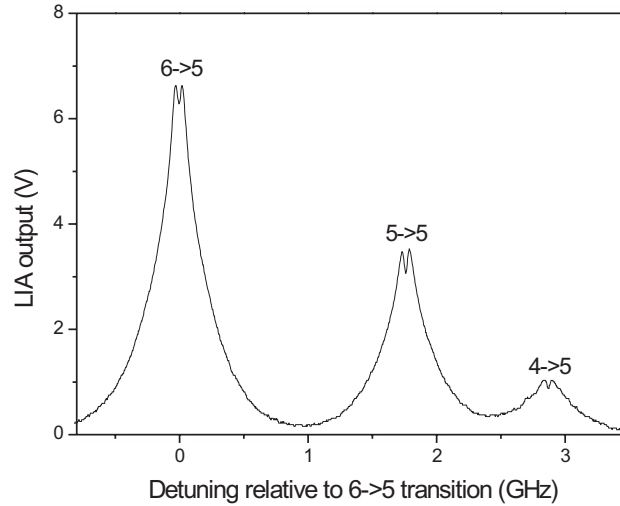


Figure 4.18: Lock-in signal for the transmission of the 451 nm light scanned across the $5^2P_{3/2}$ ($F = 4, 5, 6$) \rightarrow $6^2S_{1/2}$ ($F = 5$) transitions.

The dip at the center of each peak is found to be approximated by an inverted Lorentzian with a width of about 30 MHz. When we take this dip into account, the fit is in good agreement with the experimental data (see Figure 4.19). The dip here corresponds to an enhanced transmission of the 451 nm light, and hence it could result from the coherent population trapping or electromagnetically induced transparency in the Λ -type three level system [52, 53].

For the laser manipulation applications the 451 nm laser could be locked on the dip signal, but the effort for such stabilization scheme is relatively large. In the experiments, we lock the frequency of the Ti:Sa laser on a reference cavity. Although this method is not an absolute frequency stabilization, it reduces the long-term frequency drift and the fluctuation remains within the tolerance for the experiments.

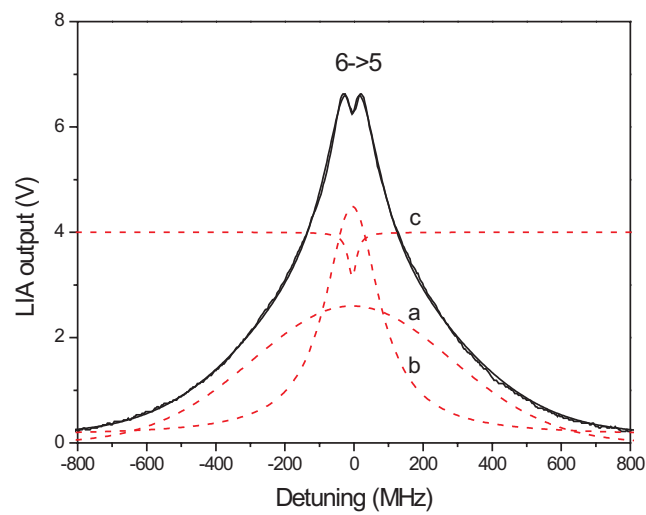


Figure 4.19: *Experimental data with least squares fit and three fit components, (a) Gaussian profile, (b) Lorentzian profile and (c) inverted Lorentzian profile. Note that the inverted Lorentzian is manually shifted up for clarity.*

Chapter 5

Opto-mechanical manipulation of an indium atomic beam

In this chapter we summarize the first experimental observations of opto-mechanical manipulation of an indium atomic beam and discuss the possible mechanisms.

5.1 Experimental set-up

The experimental set-up for laser manipulation of an indium atomic beam is drawn in Figure 5.1 (a). It can be divided into three main parts: atom source, cooling region, and probe region. The atom source consists of an indium oven heated to a temperature of 1200°C to produce the atomic beam. At this temperature, the average velocity is calculated to be 613 m/s and the most probable velocity is 565 m/s which is close to the measured 530 m/s derived from time-of-flight experiments. An aperture with a diameter of 0.5 mm is placed downstream to reduce the divergence of the atomic beam. The measured full divergence angle is about 6 mrad .

In the cooling region, the linearly polarized cooling laser beams intersect the atomic beam at 90° and then are retro-reflected by a mirror HR-coated for both 410 nm and 451 nm . In this way, a linearly polarized standing wave configuration is applied in our experiments. There is a weak magnetic field of about 1 Gauss in the cooling zone generated by a pair of coils. The direction of the magnetic field is parallel to the incident cooling laser beams.

In the probe region, the probe laser beam propagates orthogonal to the atomic beam about 632 mm away from the cooling laser beams. A CCD camera is used to record the fluorescence with spatial resolution. The typical fluorescence picture is shown in

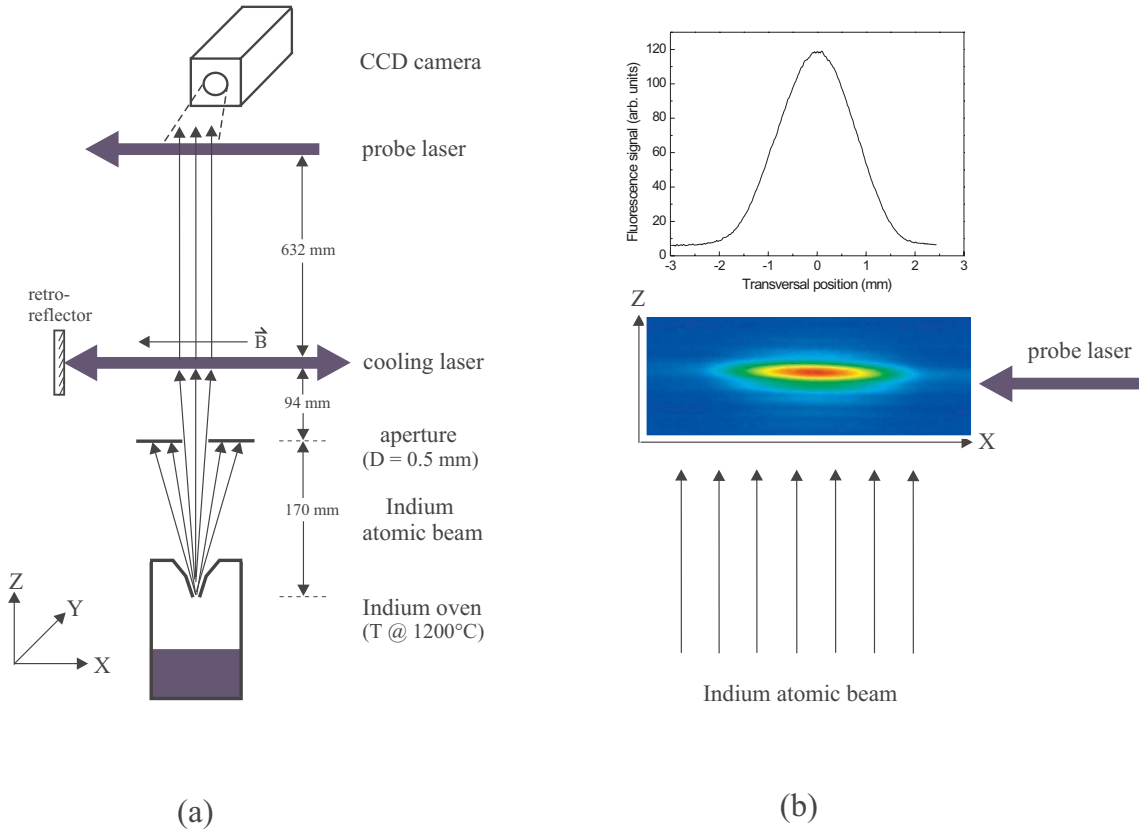


Figure 5.1: (a) *Experimental set-up for laser manipulation of an indium atomic beam. The retro-reflector is HR-coated for both 410 nm and 451 nm light. A magnetic field of 1 Gauss is generated by a pair of coils and its direction is parallel to the cooling laser beams.* (b) *The typical recorded fluorescence picture by the CCD camera. The fluorescence profile is obtained by summing up the signal strengths of each row along z direction across the fluorescence.*

Figure 5.1 (b). By summing up the signal strengths of each row along z direction across the fluorescence, the fluorescence signal is obtained for analysis (see Figure 5.1 (b)). The x axis of the graph of the fluorescence signal represents the transversal position along x direction, wherein the position 0 represents the center of the atomic beam.

5.2 Experimental observations

As discussed in Chapter 2, we use two wavelengths for the Λ -type energy level system. One at 410 nm to excite the $5^2\text{P}_{1/2} \rightarrow 6^2\text{S}_{1/2}$ transition, and another one at 451 nm to excite the $5^2\text{P}_{3/2} \rightarrow 6^2\text{S}_{1/2}$ transition.

5.2.1 Opto-mechanical effects with 410 nm and 451 nm lasers

5.2.1.1 Red-detuned 410 nm and 451 nm lasers

In order to obtain conventional Doppler cooling (see chapter 2.2), we red-detune two diode lasers exciting the $F=4 \rightarrow 5$ and $F=5 \rightarrow 5$ hyperfine transitions at 410 nm, respectively, and set the 451 nm laser on resonance (see Figure 5.2 (a)). For the probe beam, we use a third diode laser exciting the $F=4 \rightarrow 5$ transition at 410 nm. In the experiment, all lasers have a linear polarization. The fluorescence signal of the atomic beam is shown in Figure 5.2 (b) with a detuning of -1.5Γ and an intensity of about 310 mW/cm^2 for both red-detuned lasers. Surprisingly, it shows a dip at the center of the fluorescence profile, implying that the atoms are pushed away from the center of the atomic beam.

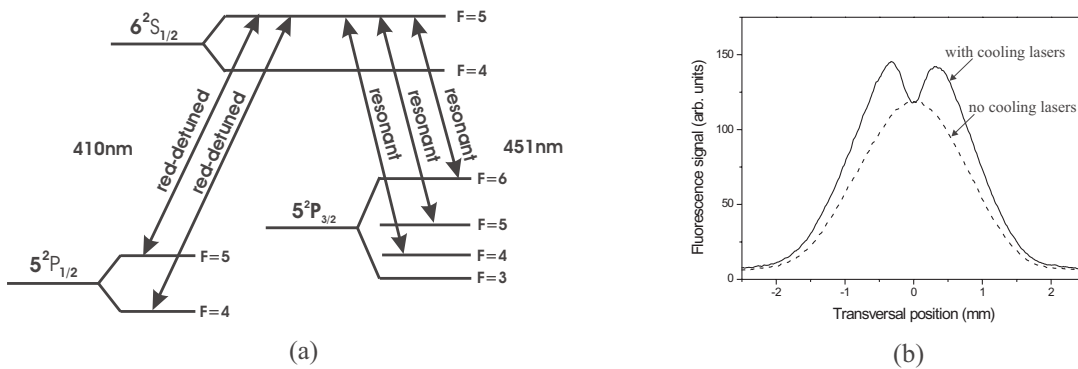


Figure 5.2: (a) The transition scheme with relevant light fields. (b) Fluorescence profiles obtained in the probe zone with the probe transition $F=4 \rightarrow 5$ at 410 nm. The dashed and solid lines show the signal without and with the cooling lasers, respectively.

Next, we red-detune the 451 nm laser by -1.2Γ ($I = 75 \text{ mW/cm}^2$ for each transition) and set two diode lasers on resonance (see Figure 5.3 (a)), the result shows the same effect with the $F=4 \rightarrow 5$ probe transition at 410 nm, i.e., there is a dip at the center of the fluorescence profile, but the signal is much weaker than that without the cooling lasers (see Figure 5.3 (b)). This is because one of the resonant 410 nm lasers pumps away the atoms from the $5^2P_{1/2}$ ($F=4$) state, which is the state being probed.

While the experiments demonstrate the opto-mechanical interaction between the light fields and the indium atoms, the observation contradicts our expectation, i.e., to find beam narrowing for red detuning.

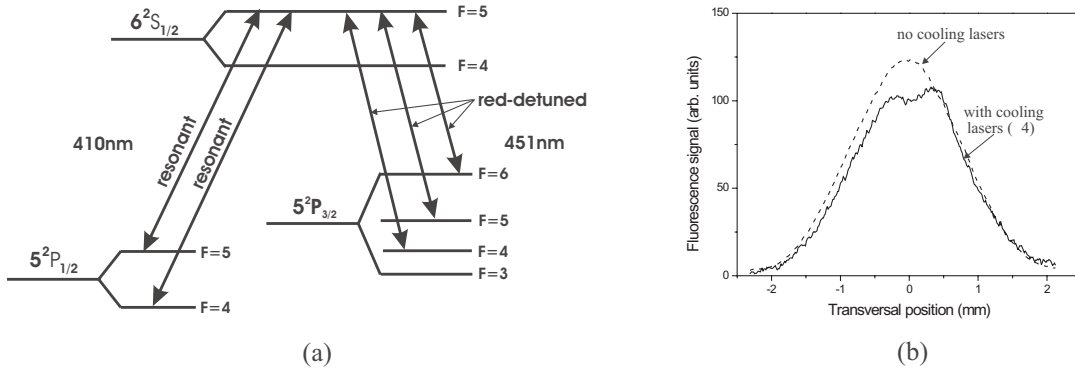


Figure 5.3: (a) The transition scheme with relevant light fields. (b) Fluorescence profiles obtained in the probe zone with the $F = 4 \rightarrow 5$ probe transition at 410 nm. The dashed line shows the signal without the cooling lasers, and the solid line is the signal (amplified by a factor of 4 for the sake of clarity) with the cooling lasers.

5.2.1.2 Blue-detuned 410 nm and 451 nm lasers

In the next step, it is natural to use blue-detuned lasers rather than the red-detuned ones. In the experiments, the probe laser again excites the $F = 4 \rightarrow 5$ transition at 410 nm. When we blue-detune the two diode lasers by $+2.5\Gamma$ and set the 451 nm laser on resonance, the result shows a peak at the center of the fluorescence profile, indicating that the atoms are pushed towards the center of the atomic beam (see Figure 5.4 (a)). The same effect is observed by blue-detuning the 451 nm laser by about $+1.2\Gamma$ and setting two diode lasers on resonance (see Figure 5.4 (b)).

5.2.2 Opto-mechanical effects with two 410 nm lasers

We have performed the experiments with two diode lasers only (see Figure 5.5 (a)). In this case the Λ -type energy level system is not closed and there exists a loss channel to the $5P_{3/2}^2$ state. To our surprise, we still find significant opto-mechanical effects. In the experiments, the $F = 4 \rightarrow 5$ hyperfine transition at 410 nm is again used as the probe transition. By blue-detuning two lasers by $+2.5\Gamma$, it shows a narrow peak at the center of the fluorescence profile, but the fluorescence signal is much weaker than that with the resonant 451 nm light (see Figure 5.5 (b)). This is because the atoms decayed to the $5P_{3/2}^2$ state are no longer pumped back to the $5P_{1/2}^2$ ($F = 4$) probe state.

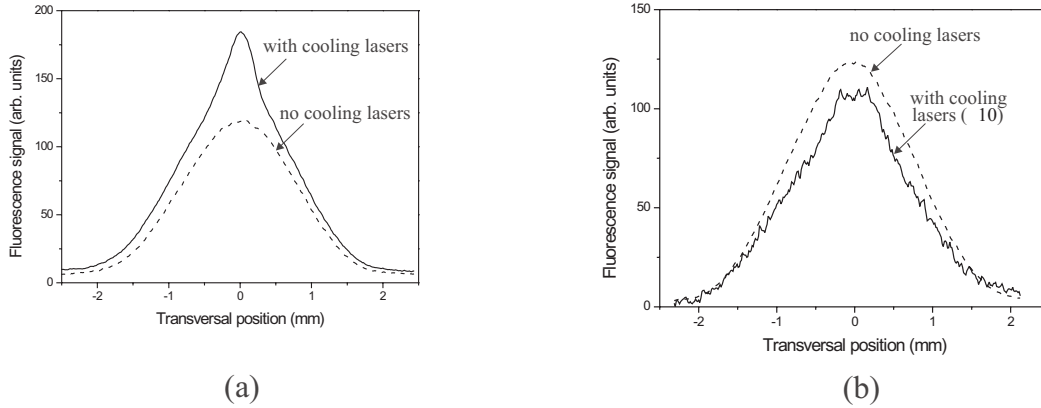


Figure 5.4: Fluorescence profiles in the probe zone with the probe transition $F=4 \rightarrow 5$ at 410 nm. The dashed and solid lines in both graphs show the signals without and with the cooling lasers, respectively. (a) The 410 nm lasers are blue detuned and 451 nm laser is set on resonance. (b) The 451 nm laser is blue detuned and 410 nm lasers are on resonance. The signal with the cooling lasers are amplified by a factor of 10 for the sake of clarity.

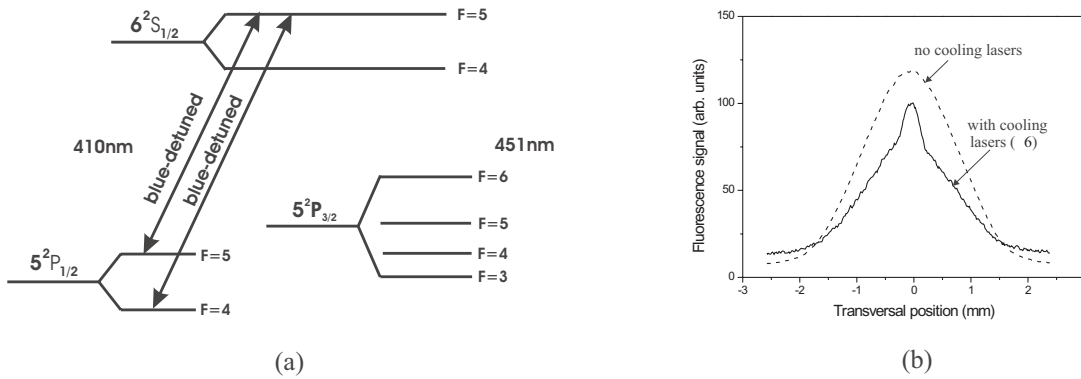


Figure 5.5: (a) The transition scheme with relevant light fields. (b) Fluorescence profiles obtained in the probe zone with the probe transition $F=4 \rightarrow 5$ at 410 nm. The dashed line shows the signal without the cooling lasers, and the solid line is the signal (amplified by a factor of 6 for the sake of clarity) with the cooling lasers.

5.2.3 Opto-mechanical effects with one 410 nm laser

Since the beam narrowing is observed with only two blue-detuned diode lasers in a non-closed Λ -type energy level system in the absence of 451 nm laser, it is interesting to observe

the effects with only one diode laser. This set-up is the simplest possible configuration for the investigation of the opto-mechanical interaction between the light fields and the indium atoms.

5.2.3.1 $F = 4 \rightarrow 5$ cooling transition

Experimental observations

In the experiments, we use the $F = 4 \rightarrow 5$ hyperfine transition at 410 nm as the cooling transition. With a blue detuning of $+2.6\Gamma$ and an laser intensity of 310 mW/cm^2 , it still shows a narrow peak at the center of the fluorescence profile for the probe transition $F = 4 \rightarrow 5$ at 410 nm (see Figure 5.6 (b)).

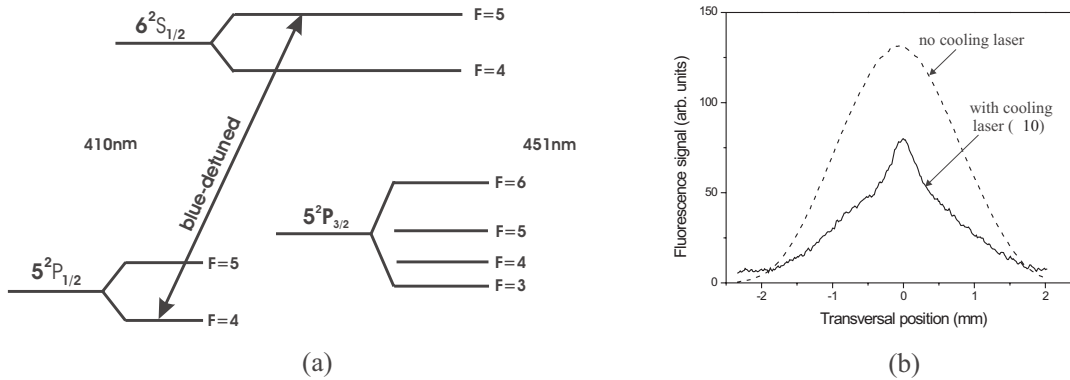


Figure 5.6: (a) The transition scheme with relevant light field. (b) The fluorescence profiles in the probe zone with the probe transition $F = 4 \rightarrow 5$ at 410 nm for a blue-detuned cooling laser. The dashed line shows the signal without the cooling laser, and the solid line is the signal (amplified by a factor of 10 for the sake of clarity) with the cooling laser.

Discussion of the shape of the fluorescence profile

In this set-up employing only one cooling laser, optical pumping can not be ignored. With the measured full divergence of the atomic beam (6 mrad) and the most probable longitudinal velocity of 565 m/s, the maximum transverse velocity is roughly calculated to be 1.7 m/s corresponding to a frequency of 4 MHz which is smaller than the natural linewidth (25 MHz) and the laser linewidth (10 MHz). Thus, optical pumping has a homogenous influence on the whole fluorescence profile and this influence is independent on the sign of the detuning, i.e., the shape of the fluorescence profile should be the same no matter whether the cooling laser is blue-detuned or red-detuned. We perform the experiment by

red-detuning the laser by the same amount as that in the experiment with blue-detuned laser. It shows a different fluorescence profile from the one with blue-detuned laser (see Figure 5.7 (b)), implying that the observed peak with blue-detuned laser does not result from optical pumping.

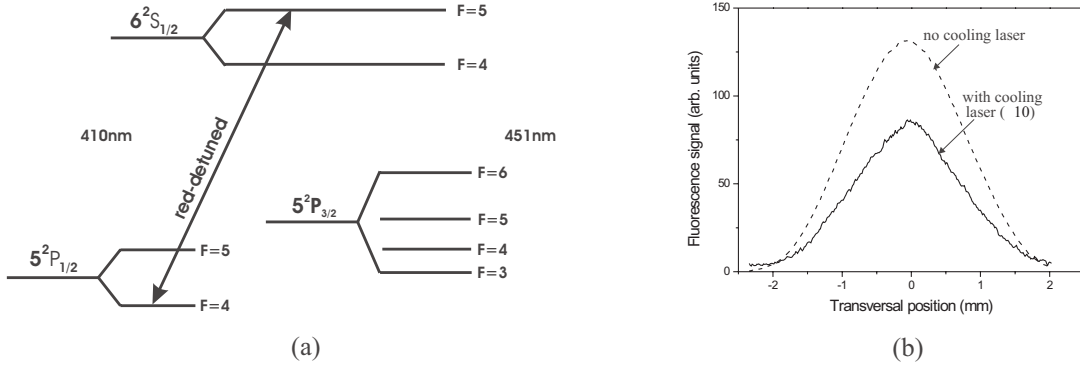


Figure 5.7: (a) The transition scheme with relevant light field. (b) The fluorescence profiles in the probe zone with the probe transition $F=4 \rightarrow 5$ at 410 nm for a red-detuned cooling laser ($\Delta = -2.6\Gamma$). The dashed line shows the signal without the cooling laser, and the solid line is the signal (amplified by a factor of 10 for clarity) with the cooling laser.

Next, we perform the experiments by again blue-detuning the cooling laser exciting the $F=4 \rightarrow 5$ hyperfine transition at 410 by $+2.6\Gamma$, but detecting the atoms in the $5P_{1/2}^2$ ($F=5$) ground states. In the experiments, the atoms in other ground states are optically pre-pumped to the $5P_{1/2}^2$ ($F=4$) ground state of the cooling transition with the resonant 410 nm laser coupling the $F=5 \rightarrow 5$ hyperfine transition and the resonant 451 nm laser coupling the $F=4,5,6 \rightarrow 5$ hyperfine transitions. The pre-pumping laser beams travel orthogonally through the atomic beam only once. The result shows again a peak at the center of the fluorescence profile (see Figure 5.8 (b)), indicating that there really exists the opto-mechanical interaction between the light fields and the indium atoms with only one laser in the presence of lots of loss channels.

5.2.3.2 $F=5 \rightarrow 5$ and $F=5 \rightarrow 4$ cooling transitions

We have observed the opto-mechanical effects with the $F=4 \rightarrow 5$ transition with one laser only. To investigate if the same effects can also be observed with other transitions, we use the $F=5 \rightarrow 5$ and $F=5 \rightarrow 4$ hyperfine transitions as the cooling transition, respectively (see Figure 5.9 (a)). In the experiments, the atoms in other ground states are optically

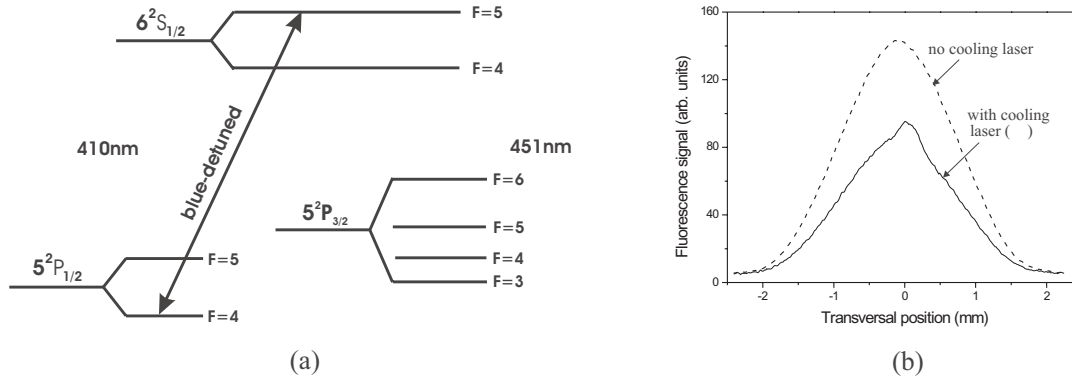


Figure 5.8: (a) The transition scheme with relevant light field. (b) Fluorescence profiles in the probe zone with the probe transition $F = 5 \rightarrow 4$ at 410 nm for a blue-detuned cooling laser. The dashed line shows the signal without the cooling laser, and the solid line is the signal (amplified by a factor of 2 for clarity) with the cooling laser.

pre-pumped to the corresponding ground state of the cooling transition with the resonant 410 nm and 451 nm lasers, which travel orthogonally through the atomic beam only once. For the probe light, all five transitions ($F = 4, 5 \rightarrow 5$ at 410 nm and $F = 4, 5, 6 \rightarrow 5$ at 451 nm) are simultaneously used. By setting the cooling laser blue-detuned by $+2.6 \Gamma$ ($I = 310 \text{ mW/cm}^2$), it shows a peak at the center of each fluorescence profile (see Figure 5.9 (b)), indicating that there also exists the opto-mechanical effects with the $F = 5 \rightarrow 5$ and $F = 5 \rightarrow 4$ transitions.

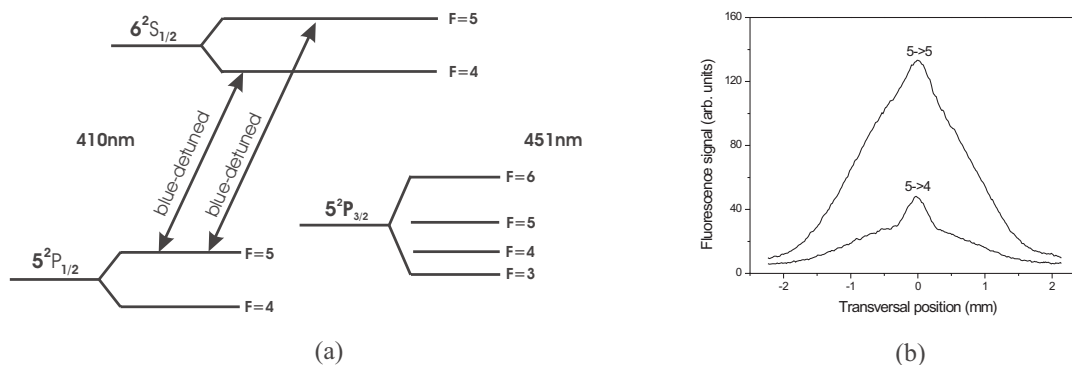


Figure 5.9: (a) The transition scheme with relevant light fields. In each experiment only one transition is used. (b) Fluorescence profiles in the probe zone with five probe transitions at both 410 nm and 451 nm.

5.3 Discussion of the possible mechanisms

We have observed opto-mechanical manipulation of the indium atomic beam with both 410 nm and 451 nm lasers, two 410 nm lasers only and one 410 nm laser only in the standing wave configuration. The observed effects show beam narrowing with blue-detuned lasers which contradicts the conventional Doppler cooling requiring the red-detuned lasers, implying that our observed effects arise from other mechanisms. The possible mechanisms include stimulated emission cooling, adiabatic cooling and bichromatic cooling.

5.3.1 Stimulated emission cooling

The stimulated emission cooling utilizes the dipole force in an intense blue-detuned standing wave [17, 54, 55]. In the dressed-atom picture, the energies of the dressed states, which are the eigenstates of atom-laser field system, oscillate periodically in space (see Figure 5.10). At nodes, the dressed states $|1, n\rangle$ and $|2, n\rangle$ coincide with the unperturbed states $|g, n+1\rangle$ and $|e, n\rangle$, respectively. Out of nodes, the dressed states are the linear combination of $|g, n+1\rangle$ and $|e, n\rangle$, and they have the maximum splitting at the antinodes. An atom in the state $|1, n\rangle$ or $|2, n\rangle$ can spontaneously decay to the state $|1, n-1\rangle$ or $|2, n-1\rangle$. The rates of spontaneous emission vary in space. If the atom is in the state $|1, n\rangle$, its decay rate is zero at the node where $|1, n\rangle = |g, n+1\rangle$ and maximum at the antinode. On the contrary, for an atom in the state $|2, n\rangle$, the decay is maximum at the nodes. Assuming an atom moves starting from the node of the standing wave in state $|1, n+1\rangle$, it will climb uphill until it reaches the potential top where the decay rate is maximum. The atom may jump either to the state $|1, n\rangle$, in which case nothing changes from the mechanical viewpoint, or to the state $|2, n\rangle$, and the atom is again in the valley, then it will climb up again until it reaches top where the $|2, n\rangle$ state is most unstable. The simulation shows that the heating induced by the spontaneous emission is negligible [54]. Thus, on the average atoms will lose kinetic energy and are slowed down.

The transition scheme of using one 410 nm cooling laser for the laser manipulation can be approximated as a two-level system, which allows us to calculate the dipole force with a simple two-level model [56]. Figure 5.11 (a) shows the calculated force with a saturation parameter of $s_0 = 6$ and a detuning of 2.6Γ which are the experimental parameters. The calculation shows no clear dipole force near zero velocity, which is the friction force with opposite direction to the velocity of the atoms. If we use a higher saturation parameter of $s_0 = 100$ and the same detuning in the calculation, a clear dipole force appears near zero velocity (see Figure 5.11 (b)), indicating that the dipole force in this cooling scheme is strongly dependent on the intensity of the cooling laser. Thus, the laser intensity in our

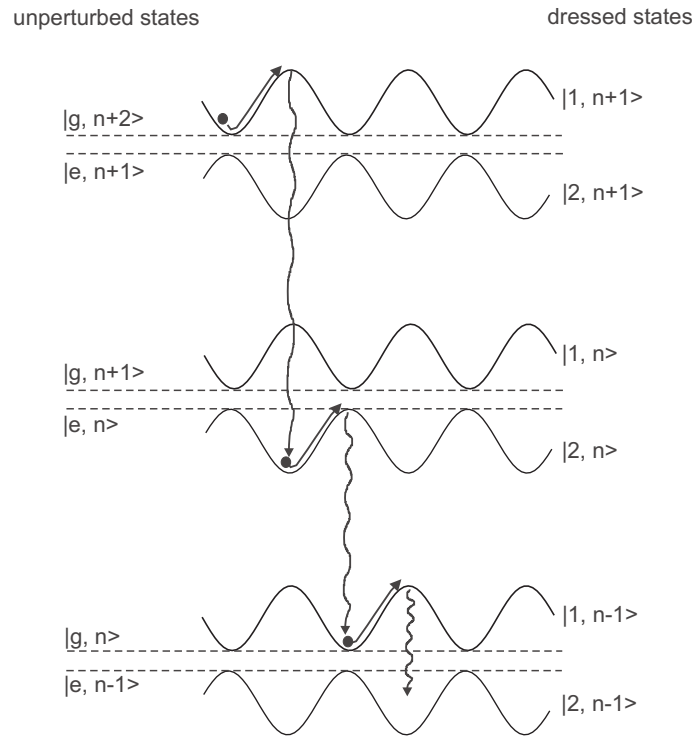


Figure 5.10: The scheme of stimulated emission cooling in an intense blue-detuned standing wave. The dashed lines represent the unperturbed states at the nodes, and the solid lines are the dressed states.

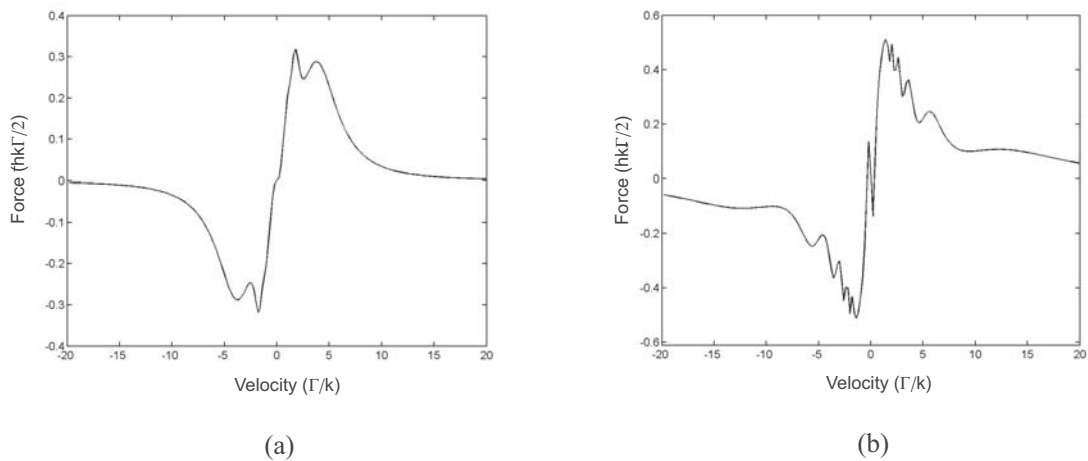


Figure 5.11: Calculated dipole force based on a two-level model for (a) $s_0 = 6$ and $\Delta = 2.6\Gamma$, and (b) $s_0 = 100$ and $\Delta = 2.6\Gamma$.

experiments could be not high enough to create such a dipole force for beam narrowing.

5.3.2 Adiabatic cooling

Due to the interaction between the atoms and the laser field, the atoms experience force in a periodic, spatially varying potential of a standing wave (see Figure 5.12) [57]. For a blue-detuned standing wave, the atoms will be attracted to the nodes of the standing wave. Those atoms with a kinetic energy less than the potential energy will be trapped around the nodes of the standing wave, and their kinetic energy may be reduced by adiabatically lowering the intensity of the standing wave, i.e., the potential energy. This scheme requires a laser beam having an intensity profile of slowly decreasing intensity along the flight direction of the atomic beam. Thus, the effect strongly depends on the intensity profile of the laser beam. In the experiments, we slowly move a blade to block the tail of the laser beam along the opposite direction to the flight direction of the atomic beam, but no obvious change in the fluorescence profile is observed.

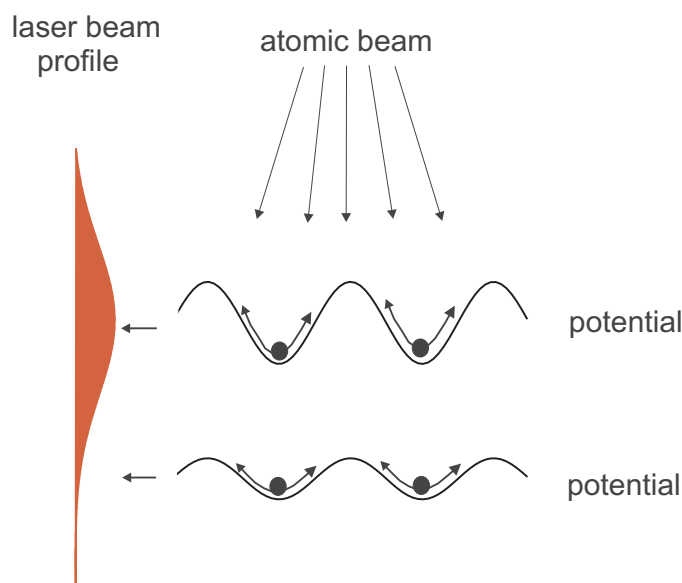


Figure 5.12: *The scheme of adiabatic cooling. The laser beam has a profile of slowly decreasing intensity along the flight direction of the atomic beam, giving rise to a slowly decreasing potential energy.*

5.3.3 Bichromatic cooling

The bichromatic cooling utilizes two pairs of blue-detuned standing-waves [58]. In this scheme, two transitions have different ground states but the same excited state (Fi-

figure 5.13). With a relative phase of π with respect to each other, the antinodes of one standing wave corresponds to the nodes of another standing wave, i.e., light shift potential hill of one ground state corresponds to the potential valley of another ground state. The atoms climb up the potential hill of one state, and are optically pumped to the potential valley of another state. From there, the same sequence is repeated. The effect of this scheme is very sensitive to the relative phase between two standing waves. In our case, the spatial period of the phase variation is about 1.3 cm for a frequency difference of 11.4 GHz between $F = 4$ and $F = 5$ states. In the experiments, we move the retro-reflector to alter this phase, but no substantial change in the signal is observed.

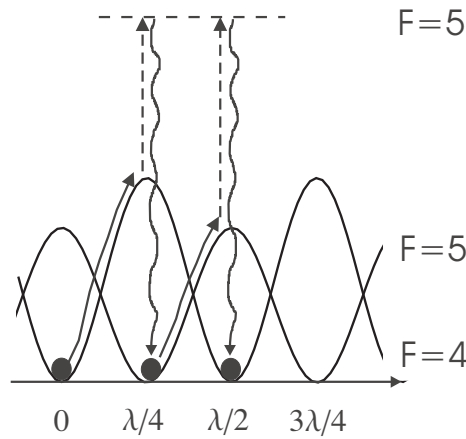


Figure 5.13: *Bichromatic cooling with two pairs of blue-detuned standing-waves. The relative phase between two standing waves is π , and hence the antinodes of one standing wave corresponds to the nodes of another standing wave.*

5.4 Discussion of achieving Doppler cooling

To achieve Doppler cooling, the atoms must absorb as many as possible photons from the cooling lasers to have a significant change in the velocity, which requires enough interaction length along with enough laser intensity. Theoretically, the maximum damping rate is obtained for $\Delta = -\Gamma/2$ and $s_0 = 2$ [59]. The minimum damping time is calculated to be about $40 \mu\text{s}$ for indium, corresponding to a minimum damping length of about 2.3 cm for atoms with the most probable velocity. However, such requirements on the laser intensity and the interaction length can not be simultaneously satisfied in our case. Thus, we must either increase the output power of the lasers, especially the 451 nm laser. This could be fulfilled by improving the frequency-doubling efficiency with other crystals, e.g. PPKTP. Or consider other schemes, which has a less requirement on the laser intensity.

One such scheme was introduced by Hoogerland *et al* [60]. The whole set-up is sketched in Figure 5.14. It consists of two mirrors tilted by a small angle α with respect to the atomic beam axis. The injected laser beam at an angle β with respect to the plane perpendicular to the atomic beam axis multiply bounces between two mirrors. With each bounce, the angle between the laser beam and the plane is reduced by an amount α . The atoms with a large incident angle are always on resonance during the whole cooling process and they can be cooled efficiently. Those with a smaller incident angle will be on resonance and cooled much later. A large capture angle and a long interaction length can be achieved with this scheme while low laser power is needed.

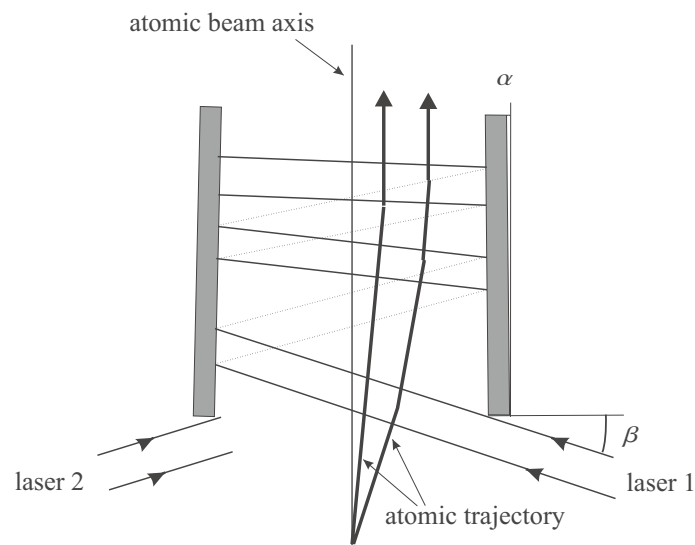


Figure 5.14: *Set-up of collimating the atomic beam with two nearly parallel mirrors.*

Chapter 6

Summary and outlook

In the frame of this thesis the experimental set-up for laser manipulation of an indium atomic beam is developed and the opto-mechanical interaction between the light fields and the indium atoms is demonstrated.

To achieve laser manipulation of the indium atoms, two wavelengths, i.e., 410 nm and 451 nm, must be used. The light sources at 410 nm are provided by GaN diode lasers, whereas light at 451 nm is acquired by frequency-doubling a Ti:Sapphire laser at 902 nm. Towards this end, a ring frequency-doubling resonator with LBO nonlinear crystal is built. The maximum output power from this cavity can reach 100 mW. To simultaneously obtain three necessary frequency components at 451 nm, a modulation scheme is utilized with the application of an electro-optical modulator (EOM) and an acousto-optical modulator (AOM). Besides the optical apparatus, a vacuum system is set up. It mainly consists of the indium atom oven, the cooling chamber and the probe chamber.

For laser manipulation, the laser frequency must be stabilized on the atomic transition frequency. This is realized through the spectroscopic technique. Therefore, different types of spectroscopy including the saturation spectroscopy and the polarization spectroscopy are performed on both the hollow cathode and the all-sapphire cell. The laser frequency is stabilized either on the Lamb-dip signal of the saturation spectroscopy or the dispersive signal of the polarization spectroscopy with the all-sapphire cell. The characterization of the frequency stabilization of the diode lasers in terms of Allan variance shows that the frequency fluctuation is much smaller than that of free-running laser, and the laser can be stabilized for at least one hour with both methods. However, due to the complicated spectroscopic scheme, the frequency of 451 nm light is stabilized on a reference cavity. Although the laser frequency is not directly stabilized on an atomic source, this method decreases the long-term frequency drift and the fluctuation falls within the tolerance for the experiments.

The experiments of laser manipulation of an indium atomic beam are performed with both 410 nm and 451 nm lasers, two 410 nm lasers only and one 410 nm laser only in the standing wave configurations. A beam narrowing is observed at the center of the atomic beam when the lasers are blue detuned and the opto-mechanical interaction between the light fields and the indium atoms is demonstrated. The observation contradicts the convention Doppler cooling, and several possible mechanisms are discussed for such laser manipulation with blue-detuned lasers.

The next experiments will mainly aim at the investigation of the cooling mechanisms and the realization of conventional Doppler cooling which provides a larger capture range. To simultaneously increase the atomic flux and reduce the divergence of the atomic beam as much as possible, a two-step collimation scheme can be applied, i.e., the atomic beam is collimated by Doppler cooling at first and then further collimated by sub-Doppler cooling. This would open the route to atomic nanofabrication with indium atomic beams.

Appendix A

Transition strengths

The relative transition rate of the m-sublevels is proportional to the matrix element for the electric dipole transition for polarization q ($q = -1, 0, 1$ for σ^- , π , σ^+ polarization):

$$\langle F', m_{F'} | \vec{d}_q | F, m_F \rangle \propto \begin{pmatrix} F' & 1 & F \\ -m_{F'} & q & m_F \end{pmatrix}^2 \langle F' || \vec{d} || F \rangle \quad (\text{A.1})$$

$$\begin{aligned} &\propto (2F + 1)(2F' + 1)(2J + 1)(2J' + 1) \cdot \\ &\cdot \begin{pmatrix} F' & 1 & F \\ -m_{F'} & q & m_F \end{pmatrix}^2 \cdot \begin{Bmatrix} L' & J' & S \\ J & L & 1 \end{Bmatrix}^2 \cdot \begin{Bmatrix} J' & F' & I \\ F & J & 1 \end{Bmatrix}^2 \end{aligned} \quad (\text{A.2})$$

with $S=1/2$ and $I=9/2$. Here F and F' are the ground and excited state, respectively. This expression is calculated for each of the possible transition combinations of m_F , $m_{F'}$, and q . The calculated values are shown in the circles of Figure A.1. To compare transitions with different F and F' , the numbers in the circles have to be multiplied by R_{411} and R_{451} . Note that these two factors are not correct for the comparison of a transition at 410 nm with a transition at 451 nm. Figure A.1 also gives the branching ratios, i.e., the probability for an excited state to decay spontaneously into the ground state, for both wavelengths.

The total relative transition rate T into any of the m states of the ground state is expressed as

$$T(F', F, J', J) \propto (2F + 1)(2F' + 1) \cdot \begin{Bmatrix} J' & F' & I \\ F & J & 1 \end{Bmatrix}^2. \quad (\text{A.3})$$

The relative transition strengths from two ground states $5^2P_{1/2}$ and $5^2P_{3/2}$ to the excited state $6^2S_{1/2}$ are calculated with this expression (see Table A.1).

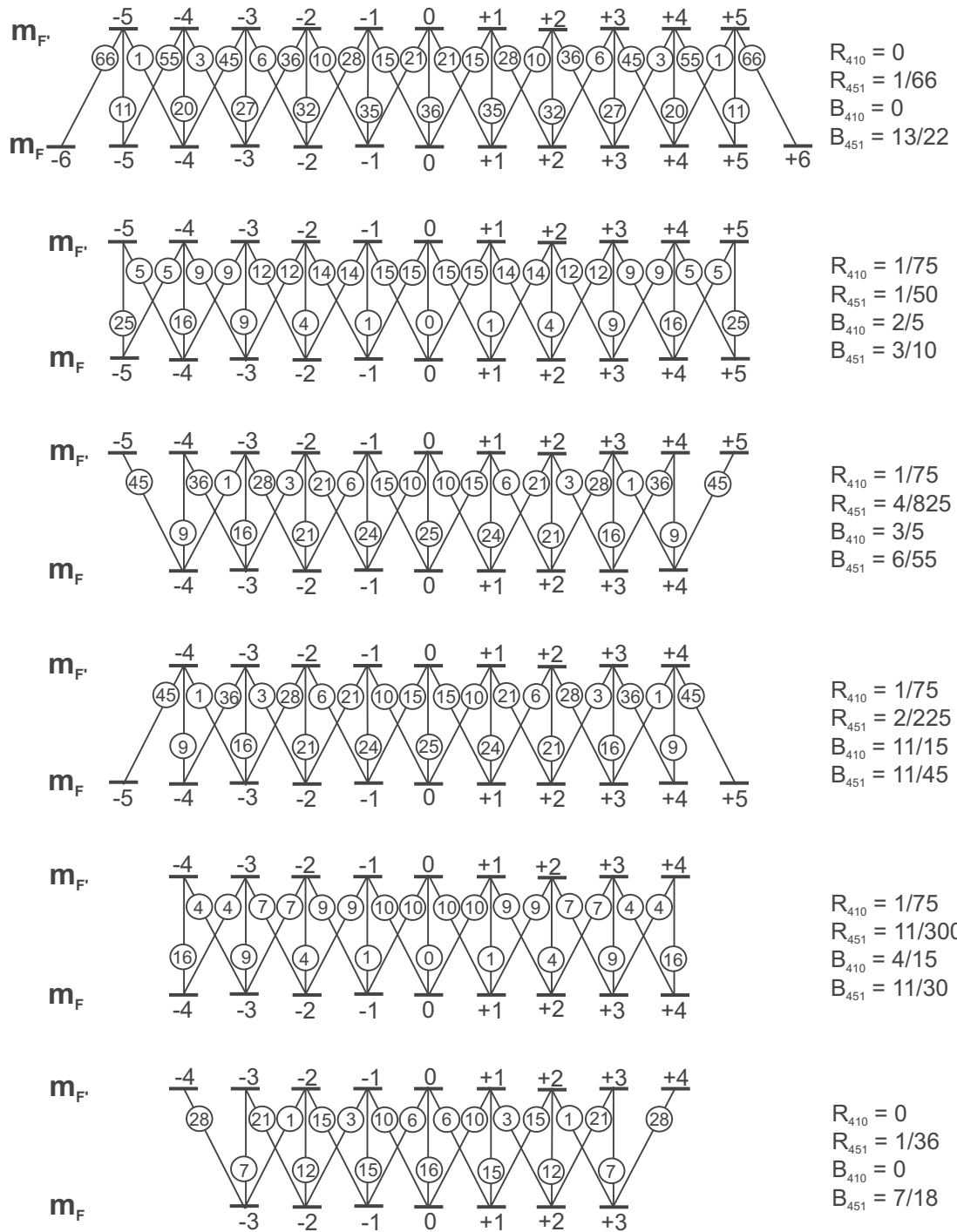


Figure A.1: The relative transition strengths of the m -sublevels for ^{115}In . R is the factor which must be multiplied when the strengths between two different transitions for each wavelength are compared.

The branching ratios B_{410} and B_{451} are then

$$B_{410}(F', F) = \frac{T(F', F, 1/2, 1/2)}{T(F', 5, 1/2, 1/2) + T(F', 4, 1/2, 1/2)} \quad (\text{A.4})$$

for transition at 410 nm and

$$B_{1_{451}}(5, F) = \frac{T(F', F, 1/2, 3/2)}{T(F', 6, 1/2, 3/2) + T(F', 5, 1/2, 3/2) + T(F', 4, 1/2, 3/2)} \quad (\text{A.5})$$

$$B_{2_{451}}(4, F) = \frac{T(F', F, 1/2, 3/2)}{T(F', 5, 1/2, 3/2) + T(F', 4, 1/2, 3/2) + T(F', 3, 1/2, 3/2)} \quad (\text{A.6})$$

for two transition groups at 451 nm.

$5^2P_{1/2} \rightarrow 6^2S_{1/2}$	relative strength T	$5^2P_{3/2} \rightarrow 6^2S_{1/2}$	relative strength T
F = 5 \rightarrow 5	22	F = 6 \rightarrow 5	65
F = 4 \rightarrow 5	33	F = 5 \rightarrow 5	33
		F = 4 \rightarrow 5	12
F = 5 \rightarrow 4	33	F = 5 \rightarrow 4	22
F = 4 \rightarrow 4	12	F = 4 \rightarrow 4	33
		F = 3 \rightarrow 4	35

Table A.1: *The relative transition strengths for Indium.*

Appendix B

Zeeman splitting

In the weak field case, the energy shift of the atomic energy levels due to Zeeman effect in a magnetic field B is given by

$$\Delta E_{FS} = g_J \mu_B B m_J , \quad (\text{B.1})$$

where $\mu_B = \frac{e\hbar}{2m_e}$ with the electron rest mass m_e is the Bohr magneton. The value of μ_B is approximately $\mu_B = 1.3996 \text{ MHz/Gauss}$. g_J is the Lande-factor expressed as

$$g_J = 1 + \frac{J(J+1) + S(S+1) - L(L+1)}{2J(J+1)} . \quad (\text{B.2})$$

g_J for the $5P_{1/2}^2$, $5P_{3/2}^2$ and $5S_{1/2}^2$ levels are listed in table B.1:

level	$5P_{1/2}^2$	$5P_{3/2}^2$	$6S_{1/2}^2$
g_J	2/3	4/3	2

Table B.1: *The Lande-factor g_J for the $5P_{1/2}^2$, $5P_{3/2}^2$ and $5S_{1/2}^2$ levels.*

Table B.2 lists the energy shift of the different levels in a magnetic field of 1 Gauss.

level	$5P_{1/2}^2$	$5P_{3/2}^2$	$6S_{1/2}^2$
$\Delta E_{FS} (m_J \cdot \text{MHz})$	0.93	1.87	2.8

Table B.2: *Energy shifts for the $5P_{1/2}^2$, $5P_{3/2}^2$ and $5S_{1/2}^2$ levels in a magnetic field of 1 Gauss.*

Similarly, the energy shift of the hyperfine energy levels in a magnetic field B is

$$\Delta E_{HFS} = g_F \mu_B B m_F \quad (\text{B.3})$$

with

$$g_F = g_J \frac{F(F+1) + J(J+1) - I(I+1)}{2F(F+1)}$$

Table B.3 lists g_F for different hyperfine energy levels

F	3	4	5	6
$g_F (5P_{1/2}^2)$		-1/15	1/15	
$g_F (5P_{3/2}^2)$	-1/2	-1/30	1/5	1/3
$g_F (6S_{1/2}^2)$		-1/5	1/5	

Table B.3: *The factor g_F for different hyperfine energy levels.*

The energy shift of the hyperfine energy levels in a magnetic field of 1 Gauss is listed in table B.4.

F	3	4	5	6
$\Delta E_{HFS} (5P_{1/2}^2) (m_F \cdot \text{MHz})$		-0.1	0.1	
$\Delta E_{HFS} (5P_{3/2}^2) (m_F \cdot \text{MHz})$	-0.7	-0.05	0.28	0.47
$\Delta E_{HFS} (6S_{1/2}^2) (m_F \cdot \text{MHz})$		-0.28	0.28	

Table B.4: *Hyperfine energy shifts for the $5P_{1/2}^2$, $5P_{3/2}^2$ and $6S_{1/2}^2$ levels in a magnetic field of 1 Gauss.*

Appendix C

Indium data

atomic mass	M	$115 \times 1.66 \cdot 10^{-27} \text{ kg}$
wavelength ($5^2P_{1/2} \longleftrightarrow 6^2S_{1/2}$)	λ	410 nm
wavelength ($5^2P_{3/2} \longleftrightarrow 6^2S_{1/2}$)	λ	451 nm
decay rate ($6^2S_{1/2} \rightarrow 5^2P_{1/2}$)	A_{410}	$2\pi \cdot 8.9 \text{ MHz}$
decay rate ($6^2S_{1/2} \rightarrow 5^2P_{3/2}$)	A_{451}	$2\pi \cdot 16.2 \text{ MHz}$
lifetime $6^2S_{1/2}$	τ	6.33 ns
linewidth $6^2S_{1/2}$	Γ	$2\pi \cdot 25.1 \text{ MHz}$
saturation intensity ($5^2P_{1/2} \longleftrightarrow 6^2S_{1/2}$)	I_0	16.9 mW/cm ²
saturation intensity ($5^2P_{3/2} \longleftrightarrow 6^2S_{1/2}$)	I_0	23.1 mW/cm ²
recoil velocity	v_{410}	8.46 mm/s
recoil velocity	v_{451}	7.69 mm/s
recoil frequency	f_{410}	10.32 kHz
recoil frequency	f_{451}	9.53 kHz
Doppler temperature	$T_{Doppler}$	600 μK

Table C.1: *Some physical data for the ^{115}In atoms.*

References

- [1] O. Stern. Der Weg zur experimentellen Prüfung der Richtungsquantelung im Magnetfeld. *Z. Phys.*, **7**, 249-253, 1921.
- [2] W. Gerlach and O. Stern. Der experimentelle Nachweis des magnetischen Moments des Silberatoms. *Z. Phys.*, **8**, 110-111, 1921.
- [3] T. Hänsch, A. Schawlow. Cooling of gases by laser radiation. *opt. Commun.*, **13**, 68-69, 1975.
- [4] D. Wineland, H. Dehmelt. *Bull. Am. Phys. Soc.*, **20**, 637, 1975.
- [5] J. Dalibard, C. Cohen-Tannoudji. Laser cooling below the Doppler limit by polarization gradients: simple theoretical models. *J. Opt. Soc. Am. B*, **6**, 2023-2045, 1989.
- [6] P. J. Ungar, D. S. Weiss, E. Riis, and S. Chu. Optical molasses and multilevel atoms: theory. *J. Opt. Soc. Am. B*, **6**, 2058-2071, 1989.
- [7] F. Lison, P. Schuh, D. Haubrich, and D. Meschede. High brilliance Zeeman-slowed cesium atomic beam. *Phys. Rev. A*, **61**, 1-9, 2000.
- [8] G. Timp, R. E. Behringer, D. M. Tennant, and J. E. Cunningham. Using light as a lens for submicron, neutral-atom lithography. *Phys. Rev. Lett.*, **69**, 1636-1639, 1992.
- [9] R. Gupta, J. J. McClelland, Z. J. Jabbour, and R. J. Celotta. Nanofabrication of a two-dimensional array using laser-focused atomic deposition. *Appl. Phys. Lett.*, **67**, 1378-1380, 1995.
- [10] Th. Schulze, B. Brezger, R. Mertens, M. Pivk, T. Pfau, and J. Mlynek. Writing a superlattice with light forces. *Appl. Phys. B*, **70**, 671-674, 2000.
- [11] T. Mütter, Th. Schulze, D. Jürgens, M. K. Oberthaler, and J. Mlynek. Three dimensional nanolithography with light forces. *Microelectronic Engineering*, **57-58**, 857-863, 2001.

- [12] J. Emsley. The Elements. Clarendon Press, Oxford. 1989.
- [13] A. N. Nesmeyanov. Vapor Pressure of Chemical Elements. Elsevier Publishing Company, New York. 1963.
- [14] J. H. M. Neijzen, A. Dönselmann. Hyperfine structure and isotope shift measurements in neutral gallium and indium with a pulsed dye laser. *Physica* **98 C**, p.235, 1980.
- [15] NIST atomic spectra database :
http://www.physics.nist.gov/cgi-bin/AtData/main_asd.
- [16] C. Cohen-Tannoudji, W. D. Phillips. New mechanisms for laser cooling. *Physics Today*, **43**, 33-40, 1990.
- [17] J. Dalibard, C. Cohen-Tannoudji. Dressed-atom approach to atomic motion in laser light: the dipole force. *J. Opt. Soc. Am. B*, **2**, 1707-1720, 1990.
- [18] J. J. McClelland. Atom-optical properties of a standing-wave light field. *J. Opt. Soc. Am. B*, **12**, 1761-1768, 1995.
- [19] V. I. Balykin, V. S. Letokhov. The possibility of deep laser focusing of an atomic beam into the \dot{A} -region. *Opt. Commun.*, **64**, 151-156, 1987.
- [20] V. Natarajan, R. E. Behringer, and G. Timp. High-contrast, high-resolution focusing of neutral atoms using light forces. *Phys. Rev. A*, **53**, 4381-4385, 1995.
- [21] G. Timp, R. E. Behringer, D. M. Tennant, J. E. Cunningham, M. Prentiss, and K. K. Berggren. Using light as a lens for submicron, neutral-atom lithography. *Phys. Rev. Lett.*, **69**, 1636-1639, 1992.
- [22] J. J. McClelland, R. E. Scholten, E. C. Palm, and R. J. Celotta. Laser-focused atomic deposition. *Science*, **262**, 877-880, 1993.
- [23] S. Nakamura, G. Fasol. The Blue Laser Diode. Springer, Berlin, 1997.
- [24] <http://cfa-www.harvard.edu/HITRAN/>
- [25] M. C. Teich, B. E. A. Saleh. Fundamentals of photonics. John Wiley & Sons, Inc., New York, 1991.
- [26] R. W. Bory. Nonlinear optics. Academic Press, San Diego, 1992.
- [27] J. Q. Yao, T. S. Fahlen. Calculatin of optimum phase match parameters for the biaxial crystal KT_iOPO_4 . *J. Appl. Phys.*, **55**, 65-70, 1984.

- [28] A. Yariv. Optical Electronics. Fourth edition, Saunders College Publishing, New York, 1991.
- [29] C. Chen, Y. Wu, A. Jiang, B. Wu, G. You, R. Li and S. Lin. New nonlinear-optical crystal: LiB_3O_5 . *J. Opt. Soc. Am. B*, **6**, 616, 1989.
- [30] notes in <http://www.castech.com/doce/LBO.htm>
- [31] G. D. Boyd, D. A. Kleiman. Parametric interaction of focused gaussian light beams. *J. Appl. Phys.*, **39**, P.3597, 1968.
- [32] R. Wynands. Frequenzmessung und -synthese mit Halbleiterlasern. Dissertation, Ludwig-Maximilians-Universität München, 1988.
- [33] A. Ashkin, G. D. Boyd, J.M. Dziedzic. Resonant optical second harmonic generation and mixing. *IEEE J. Quan. Elec.*, **QE-2**, 109-123, 1966.
- [34] F. A. Jenkins, H.E. White. Fundamentals of optics. MacGraw Hill, New York, P.65, 1957.
- [35] D. C. Hanna. Astigmatic gaussian beams produced by axially asymmetric laser cavities. *IEEE J. Quan. Elec.*, **QE-5**, 483-488, 1969.
- [36] T. W. Hänsch, B. Couillaud. Laser frequency stabilization by polarization spectroscopy of a reflecting reference cavity. *Opt. Commun.*, **35**, 441-444, 1980.
- [37] A.D. White. Frequency stabilization of gas lasers. *IEEE J. Quan. Elec.*, **QE-1**, 349-357, 1965.
- [38] R. W. P. Drewer, J. L. Hall, F. V. Kowalski, J. Hough, G. M. Ford, A. J. Munley, and H. Ward. Laser phase and frequency stabilization using an optical resonator. *Appl. Phys. B*, **31**, 97-105, 1983.
- [39] R. C. Jones. New calculus for the treatment of optical systems. *J. Opt. Soc. Am.*, **31**, 488, 1941.
- [40] W. Demtröder. Laserspektroskopie, 3 Auflage. Springer Verlag, Berlin, Heidelberg, New York.
- [41] P. W. Smith, T. W. Hänsch. Cross-relaxation effects in the saturation of the 6328-Å neon-lase line. *Phys. Rev. Lett.*, **26**, 740-743, 1971.
- [42] C. Wieman, T. W. Hänsch. Doppler-free laser polarization spectroscopy. *Phys. Rev. Lett.*, **36**, 1170-1172, 1976.

- [43] R. E. Teets, F. V. Kowalski, W. T. Hill, N. Carlson and T. W. Hänsch. Laser polarization spectroscopy. *Proc. SPIE*, **113**, 80, 1977.
- [44] C. P. Pearman, C. S. Adams, S. G. Cox, P. F. Griffin, D. A. Smith and I. G. Hughes. Polarization spectroscopy of a closed atomic transition: applicatins to laser frequency locking. *J. Phys. B*, **35**, 5141-5151, 2002.
- [45] X. Chen, V. L. Telegdi, and A. Weis. Magneto-optical rotation near the caesium D2 line (Macaluso-Corbino effect) in intermediate fields: I. Linear regime. *J. Phys. B*, **20**, 5653-5662, 1987.
- [46] U. Rasbach, J. Wang, R. dela Torre, V. Leung, B. Klöter, and D. Meschede; T. Varzhapetyan, and D. Sarkisyan. One- and two-color laser spectroscopy of Indium vapor in an all-sapphire cell. Submitted to *Phys. Rev. A* on May 21. 2004.
- [47] A. Weis, J. Wurster, and S. I. Kanorsky. Quantitative interpretation of the nonlinear Faraday effect as Hanle effect of a light-induced birefringence. *J. Opt. Soc. Am. B*, **10**, 716-724, 1993.
- [48] D. W. Allan. Statistics of atomic frequency atandards. *Proc. IEEE*, **54**, 221-230, 1966.
- [49] C. Brechignac and R. Vetter. Study of velocity-changing collisions in excited Kr using saturation spectroscopy. *Phys. Rev. A*, **17**, 1609-1613, 1977.
- [50] J. Tenenbaum, E. Miron, S. Lavi, J. Liran, M. Strauss, J. Oreg, and G. Erez. Velocity changing collisions in saturation absorption of U. *J. Phys. B: At. Mol. Phys.*, **16**, 4543-4553, 1983.
- [51] A. Gallagher, and D. E. Pritchard. Exoergic collisions of cold Na* - Na. *Phys. Rev. Lett.*, **63**, 957-960, 1989.
- [52] E. Arimondo and G. Orriols. Nonabsorbing atomic coherences by coherent two-photon transitions in three-level optical pumping. *Lett. Nuovo Cimento*, **17**, 333-338, 1976.
- [53] S. E Harris. Electromagnetically induced transparency. *Physics Today*, **50**, July 1997.
- [54] A. Aspect, J. Dalibard, A. Heidmann, C. Salomon, and C. Cohen-Tannoudji. Cooling atoms with stimulated emission. *Phys. Rev. Lett.*, **57**, 1688-1691, 1986.
- [55] C. A. Sackett, J. Chen, J. J. Tollett, and R. G. Hulet. Dipole force laser cooling in multilevel atoms. *Laser Physics*, **4**, 861-865, 1994.

-
- [56] V. G. Minogin, O. T. Serimaa. Resonant light pressure forces in a strong standing laser wave. *Opt. Commun.*, **30**, 373-379, 1979.
- [57] J. Chen, J. G. Story, J. J. Tollett, and Randall G. Hulet. Adiabatic cooling of atoms by an intense standing wave. *Phys. Rev. Lett.*, **69**, 1344-1347, 1992.
- [58] R. Gupta, C. Xie, S. Padua, H. Batelaan, and H. Metcalf. Bichromatic laser cooling in a three-level system. *Phys. Rev. Lett.*, **71**, 3087-3090, 1993.
- [59] Harold J. Metcalf, P. van der Straten. Laser cooling and trapping. Springer, 1999. P.35.
- [60] M. D. Hoogerland, J. P. J. Driessen, E. J. D. Vrendenbergt, H. J. L. Megens, M. P. Schuwer, H. C. W. Beijerinck, and K. A. H. van Leeuwen. Bright thermal atomic-beams by laser cooling - A 1400-fold gain in beam flux. *App. Phys. B*, **62**, 323-327, 1996.

Acknowledgements

First, I would like to express gratitude to my advisor Prof. Dr. Dieter Meschede for his academic advisor and direction, constant encouragement during my study in Bonn. I would like to thank Prof. Dr. Karl Maier for his kind acceptance as the reference.

I would like to thank Dr. Ulrich Rasbach and Dr. Dietmar Haubrich for their helpful discussions and suggestions for the experiments, and kindness to read and correct this thesis.

My thanks are due to Ruby dela Torre for the good cooperation in the past three years in the lab and share of the happiness for every progress in the experiments, Bernhard Klöter for joining the indium lab, and also the other colleagues in the group for their tremendous help.

I am indebt to many people during my study in Bonn. First and the most important, I am extremely grateful for my parents, who have sacrificed themselves to give me the best education. I am also extremely grateful for my wife, her love and support during these years make this doctoral thesis possible. I am also very grateful for my brother who has taken the responsibility to take care of our parents while I was studying abroad.

I also would like to thank Gottlieb Daimler und Karl Benz-Stiftung for the financial support during my first year in Bonn.